SCIENCE CHINA
Mathematics

• ARTICLES •

February 2024 Vol. 67 No. 2: 431–454
https://doi.org/10.1007/s11425-022-2064-1

An oscillation-free Hermite WENO scheme for hyperbolic conservation laws

Zhuang Zhao[1] & Jianxian Qiu[2,*]

[1]*School of Mathematical Sciences and Institute of Natural Sciences, Shanghai Jiao Tong University, Shanghai* 200240*, China;*
[2]*School of Mathematical Sciences and Fujian Provincial Key Laboratory of Mathematical Modeling and High-Performance Scientific Computing, Xiamen University, Xiamen* 361005*, China*

Email: zzhao-m@sjtu.edu.cn, jxqiu@xmu.edu.cn

Received May 2, 2022; accepted November 23, 2022; published online May 24, 2023

Abstract In this paper, the sixth-order oscillation-free Hermite weighted essentially non-oscillatory (OF-HWENO) scheme is proposed for hyperbolic conservation laws on structured meshes, where the zeroth- and first-order moments are the variables for the governing equations. The main difference from other HWENO schemes existing in the literature is that we add high-order numerical damping terms in the first-order moment equations to control spurious oscillations for the OF-HWENO scheme. The OF-HWENO scheme not only can achieve the designed optimal numerical order, but also can be easily implemented as we use only one set of stencils in the reconstruction procedure and the same reconstructed polynomials are applied for the zeroth- and first-order moment equations. In order to obtain the adaptive order resolution when facing discontinuities, a transition polynomial is added in the reconstruction, where the associated linear weights can also be any positive numbers as long as their summation equals one. In addition, the OF-HWENO scheme still keeps compactness as only immediate neighbor values are needed in the space discretization. Some benchmark numerical tests are performed to illustrate the high-order accuracy, high resolution and robustness of the proposed scheme.

Keywords Hermite WENO scheme, hyperbolic conservation laws, oscillation-free, adaptive order, discontinuous Galerkin method

MSC(2020) 35L65, 65M08

Citation: Zhao Z, Qiu J X. An oscillation-free Hermite WENO scheme for hyperbolic conservation laws. Sci China Math, 2024, 67: 431–454, https://doi.org/10.1007/s11425-022-2064-1

1 Introduction

In this paper, we construct a sixth-order oscillation-free Hermite weighted essentially non-oscillatory (OF-HWENO) scheme with artificial linear weights for one- and two-dimensional hyperbolic conservation laws, where we modify the first-order moment equations by adding high-order numerical damping terms, which is different from other HWENO schemes. The idea of HWENO schemes comes from the weighted essentially non-oscillatory (WENO) schemes, which have been widely applied for solving linear and nonlinear hyperbolic conservation laws. The first WENO scheme was proposed by Liu et al. [21] based on essentially non-oscillatory (ENO) schemes [11–13] in 1994, where they gave a basic idea by nonlinearly

---

* Corresponding author

© Science China Press 2023

combining all the candidate stencils in the finite volume framework to obtain higher-order accuracy, and then in 1996, Jiang and Shu [15] proposed a fifth-order finite difference WENO scheme following [21], in which a general framework to define the smoothness indicators and nonlinear weights was presented. Since then, WENO schemes have been further developed in, for example, [2, 6, 8, 14, 16, 34, 39, 41], and a more detailed review can be seen in [27].

To both achieve high-order accuracy and keep the compactness of the WENO schemes, Qiu and Shu [24, 25], using the solution and its derivative, constructed a new type of WENO schemes, termed as Hermite WENO (HWENO) schemes, which has the fifth-order accuracy only using the immediate neighbor values in the reconstruction. Despite good performance for many benchmark problems, it gives poor resolutions for the double Mach and the step forward problems, which was solved later in [38] using a different procedure to reconstruct the derivative terms. Since the solutions of nonlinear hyperbolic conservation laws often contain discontinuities, their derivatives would become quite large near discontinuities leading to instability to some extent. Hence, many HWENO schemes [5, 20, 29, 32] were developed using different reconstructed polynomials to discretize the space for the original and derivative equations as in [24, 25, 38], but additional positivity-preserving techniques or the smaller Courant-Friedrichs-Lewy (CFL) number had to be used in these HWENO schemes. To resolve this issue, Zhao et al. [35] borrowed the thought of limiter for the discontinuous Galerkin (DG) method [7] to modify the first-order moments near discontinuities of the solution and obtained a more robust and efficient HWENO scheme, which is a moment-based HWENO scheme, and Dumbser et al. [9] gave a general and unified framework to define the moment-based numerical scheme extended from the WENO method, the HWENO method and the DG method, termed as the P_NP_M method; therefore, the HWENO scheme [35] can also be viewed as the P_1P_M method. Since then, the hybrid HWENO scheme with artificial linear weights [36], the hybrid HWENO scheme with positivity-preserving processing [10], the semi-Lagrangian hybrid HWENO scheme [37] and the Hermite TENO scheme [31] have been developed by following the idea of the hybrid HWENO scheme [35]. Recently, Li et al. [18] designed a more robust multi-resolution HWENO scheme based on the solution and its derivative directly using the reconstructed technique in the multi-resolution WENO scheme [41], which can also employ the larger CFL number and the non-additional positivity-preserving technique. However, they still modified the first-order moments near discontinuities to improve the stability and enhance the resolution in the later moment-based multi-resolution HWENO scheme [19].

In order to overcome nonphysical oscillations, the HWENO schemes listed above partly used different reconstructed polynomials to discretize the space for the original and derivative equations in [5, 20, 24, 25, 29, 32, 38], while others [10, 19, 31, 35–37] modified the first-order moments or the derivatives near discontinuities before the space reconstruction. However, the two procedures will reduce the accuracy of the reconstruction and obviously increase the computation cost if the hybrid technique is not employed. For both controlling spurious oscillations near discontinuities and maintaining the accuracy of the space reconstruction, we modify the first-order moment equations by adding high-order numerical damping terms at the cost of a little time as was done in the recent oscillation-free DG (OFDG) methods [22, 23], in which they added damping terms on high-order coefficients of the basic function in sprit to the "local projection stabilization" schemes [3, 4]. The solutions of the OFDG methods [22, 23] not only have non-physical oscillations near discontinuities but also preserve the conservation and give optimal *a priori* estimates and super-convergence as in the standard DG method [7].

In this paper, inspired by the OFDG methods [22, 23], we modify the first-order moment equations by adding high-order numerical damping terms in the OF-HWENO scheme, where the damping terms are the product of the first-order moments and the damping coefficients, which play an important role in controlling spurious oscillations. The damping coefficients only depend on the jump of the zeroth- and first-order derivatives at the interface for the reconstructed polynomial, rather than relying on the higher-order derivatives of the solution as in the OFDG methods [22, 23]. Generally speaking, the OF-HWENO scheme gets rid of oscillations by modifying the first-order moment equation and discretizes the space using the same reconstructed polynomials, which is different from the previous HWENO schemes, where some of them discretized the space using different reconstructed polynomials as in [24, 25], while others modified the first-order moments near discontinuities as was down in [35,36]. To achieve the adaptive order resolution when facing discontinuities, we add a transition cubic polynomial in the space reconstruction as the adaptive WENO schemes [1, 2] and the multi-resolution WENO/HWENO schemes [18, 19, 41], where the linear weights can be any positive numbers with the only requirement that their summation equals one as in [36]. Compared with other HWENO schemes, the advantages of the OF-HWENO scheme are that it not only controls the oscillation well but also obtains the highest theoretical order accuracy. Meanwhile, the reconstruction of OF-HWENO scheme has the adaptive order resolution when facing discontinuities, which is more robust and is with higher resolutions. Moreover, the OF-HWENO scheme is easier to implement as the space discretization uses the same reconstructed polynomials. Note that the damping terms are only added in the first-order moment equations, and the accuracy order of the damping coefficients is the same as the accuracy of the reconstruction, which is why the OF-HWENO scheme maintains the conservation and accuracy simultaneously. Since the approximation for the damping terms is linear, the calculation only adds a bit of computation time. In addition, we mention that the OF-HWENO scheme has more compact stencils and higher-order accuracy in the reconstruction than the classical fifth-order WENO scheme of Jiang and Shu [15]. In summary, the proposed OF-HWENO scheme not only preserves the conservation, compactness, robustness, and high resolution of the previous moment-based HWENO schemes [19, 35, 36], but also has higher-order accuracy both in one and two dimensions as that will be shown in the numerical tests.

The rest of this paper is organized as follows. In Section 2, we present the detailed implementation of the OF-HWENO scheme in the one- and two-dimensional cases. In Section 3, we perform some benchmark numerical tests to illustrate the numerical accuracy, high resolution, and robustness of the proposed scheme. We give concluding remarks in Section 4.

2 Description of the OF-HWENO scheme

In this section, we construct an adaptive order OF-HWENO scheme with artificial linear weights for solving hyperbolic conservation laws, which achieves the sixth-order accuracy in the smooth regions, while has the adaptive order resolution when facing discontinuities.

2.1 One-dimensional case

We first consider one-dimensional scalar hyperbolic conservation laws

$$\begin{cases} u_t + f(u)_x = 0, \\ u(x,0) = u_0(x). \end{cases} \tag{2.1}$$

For simplicity, we partition the computing domain by uniform meshes $I_i = [x_{i-1/2}, x_{i+1/2}]$, where the mesh size Δx is $x_{i+1/2} - x_{i-1/2}$ and the mesh center x_i is $\frac{x_{i-1/2}+x_{i+1/2}}{2}$.

To design an OF-HWENO scheme, we first multiply the original equation (2.1) by $\frac{1}{\Delta x}$ and $\frac{x-x_i}{(\Delta x)^2}$, respectively, then integrate them over I_i and use the numerical flux to approximate the flux $f(u)$ at the interface points. Finally, we add a damping term in the first-order moment equation and then obtain the semi-discrete finite volume OF-HWENO scheme as

$$\begin{cases} \dfrac{d\overline{u}_i(t)}{dt} = -\dfrac{1}{\Delta x}(\hat{f}_{i+1/2} - \hat{f}_{i-1/2}), \\ \dfrac{d\overline{v}_i(t)}{dt} = -\dfrac{1}{2\Delta x}(\hat{f}_{i+1/2} + \hat{f}_{i-1/2}) + \dfrac{1}{\Delta x}F_i(u) - \dfrac{\sigma_i^d}{\Delta x}\overline{v}_i(t), \end{cases} \tag{2.2}$$

where $\overline{u}_i(t) = \frac{1}{\Delta x}\int_{I_i} u dx$ and $\overline{v}_i(t) = \frac{1}{\Delta x}\int_{I_i} u \frac{x-x_i}{\Delta x} dx$ are the zeroth- and first-order moments in I_i, respectively. $\hat{f}_{i\pm1/2}$ is the numerical flux to approximate the flux $f(u)$ at $x_{i\pm1/2}$. $F_i(u)$ is the integral average value of the flux $f(u)$ in I_i, and σ_i^d is the coefficient of the damping term.

Here, we take the global Lax-Friedrichs numerical flux method as

$$\hat{f}_{i+1/2} = \frac{1}{2}(f(u^-_{i+1/2}) + f(u^+_{i+1/2})) - \frac{\alpha}{2}(u^+_{i+1/2} - u^-_{i+1/2}),$$

in which $\alpha = \max_u |f'(u)|$, and $F_i(u)$ is approximated by a four-point Gauss-Lobatto quadrature formula as

$$F_i(u) = \frac{1}{\Delta x}\int_{I_i} f(u)dx \approx \sum_{l=1}^{4} \omega_l f(u(x^G_l, t)),$$

where the weights are $\omega_1 = \omega_4 = \frac{1}{12}$ and $\omega_2 = \omega_3 = \frac{5}{12}$, and the quadrature points in I_i are

$$x^G_1 = x_{i-1/2}, \quad x^G_2 = x_{i-\sqrt{5}/10}, \quad x^G_3 = x_{i+\sqrt{5}/10}, \quad x^G_4 = x_{i+1/2},$$

in which x_{i+a} is $x_i + a\Delta x$. In terms of the OFDG method [23], $\sigma^d_i \geqslant 0$ has to be carefully chosen so that it is small in smooth regions and becomes large near discontinuities satisfying

$$\sigma^d_i = \omega^d \sum_{l=0}^{1} (2l+1)(\Delta x)^l ([\![\partial^l_x u]\!]^2_{i-1/2} + [\![\partial^l_x u]\!]^2_{i+1/2})^{\frac{1}{2}}, \tag{2.3}$$

where $[\![\partial^l_x u]\!]_{i+1/2} = \partial^l_x u(x_{i+1/2})\,|_{I_{i+1}} - \partial^l_x u(x_{i+1/2})\,|_{I_i}$, which denotes the jump of $\partial^l_x u$ at $x = x_{i+1/2}$. Here, we only need to consider the zeroth- and first-order partial derivatives of u with respect to the x variable at the interface rather than relying on the higher-order partial derivatives of the solution in the OFDG method [23]. ω^d is a free parameter, set as 3.5 for the one-dimensional case to have the high resolution and non-physical oscillations simultaneously, which is not a unique choice, and $\omega^d \in [2, 5]$ also works well in the listed numerical tests below. Particularly, if we do not add the damping term in (2.2), the scheme is a standard moment-based HWENO scheme as that in [19, 35, 36]. However, the first-order moment would bring some oscillations near discontinuities. One way to control it is to use different reconstructed methods for the original equation and the derived equations as [24, 25], while the other way is to add an HWENO limiter procedure in advance as [35, 36]. Although the above two techniques can control the non-physical oscillations well when there is a discontinuity, the accuracy of these schemes [24, 25, 35, 36] reduces to the fifth-order accuracy, and the complexity and computation time also increase obviously. Unlike them, the OF-HWENO scheme discretizes the space using the same reconstructed polynomials directly, which maintains the sixth-order accuracy and implements easily.

Remark 2.1. The damping term is added only in the first-order moment equation, which does not destroy the conservation of the scheme. In addition, the damping coefficient in (2.3) is very small in the smooth regions, and its numerical errors depend on the original scheme, while in the discontinuous regions, the damping coefficient becomes large, and the high frequency waves from the first-order moment equation are damped out as time evolves. Hence, adding the damping term does not destroy the conservation and accuracy of the original scheme and can control spurious oscillations.

For the semi-discrete OF-HWENO scheme (2.2), the most important part is the space discretization, including the HWENO reconstruction of $u^{\mp}_{i\pm1/2}$, $u_{i\pm\sqrt{5}/10}$ and the linear approximation of $[\![\partial^l_x u]\!]_{i\pm1/2}$, and the overall procedures are given as follows.

(1) The HWENO-AO(6,4,2) method for the reconstructed polynomial $u_i(x)$.

For the WENO schemes [39] and the HWENO scheme [36] with artificial linear weights, the main idea is that the reconstruction uses a nonlinear convex combination of a high degree polynomial with several low degree polynomials, but its resolution will change rapidly. Hence, we add a transition polynomial as the adaptive order WENO schemes [1, 2] and the multi-resolution WENO/HWENO schemes [18, 19, 41], and then we construct the adaptive order HWENO reconstructed method as the following steps.

Step 1. Reconstruct the approximated polynomials on the different stencils.

We first give a large stencil $S_1 = \{I_{i-1}, I_i, I_{i+1}\}$ and two small stencils $S_2 = \{I_{i-1}, I_i\}$ and $S_3 = \{I_i, I_{i+1}\}$, and then we get a quintic polynomial $q_0(x)$ and a cubic polynomial q_1 on S_1, respectively, satisfying

$$\frac{1}{\Delta x}\int_{I_{i+j}} q_0(x)dx = \overline{u}_{i+j}, \quad \frac{1}{\Delta x}\int_{I_{i+j}} q_0(x)\frac{x-x_{i+j}}{\Delta x}dx = \overline{v}_{i+j}, \quad j=-1,0,1 \tag{2.4}$$

and

$$\frac{1}{\Delta x}\int_{I_{i+j}} q_1(x)dx = \overline{u}_{i+j}, \quad j=-1,0,1, \quad \frac{1}{\Delta x}\int_{I_i} q_1(x)\frac{x-x_i}{\Delta x}dx = \overline{v}_i.$$

We can also obtain two linear polynomials $q_2(x)$ and $q_3(x)$ on S_2 and S_3, respectively, matching

$$\frac{1}{\Delta x}\int_{I_{i+j}} q_2(x)dx = \overline{u}_{i+j}, \quad j=-1,0, \quad \frac{1}{\Delta x}\int_{I_{i+j}} q_3(x)dx = \overline{u}_{i+j}, \quad j=0,1.$$

Step 2. Obtain equivalent expressions for the above reconstructed polynomials.

With the similar idea of the central WENO schemes [16,17] and the WENO/HWENO schemes [36,39] with artificial linear weights, we first rewrite $q_0(x)$ as

$$q_0(x) = \gamma_0^H\left(\frac{1}{\gamma_0^H}q_0(x) - \frac{\gamma_1^H}{\gamma_0^H}q_1(x)\right) + \gamma_1^H q_1(x), \tag{2.5}$$

and then rewrite $q_1(x)$ as

$$q_1(x) = \gamma_1^L\left(\frac{1}{\gamma_1^L}q_1(x) - \sum_{l=2}^{3}\frac{\gamma_l^L}{\gamma_1^L}q_l(x)\right) + \sum_{l=2}^{3}\frac{\gamma_l^L}{\gamma_1^L}q_l(x), \tag{2.6}$$

where the above equations (2.5) and (2.6) are always satisfied with $\gamma_0^H \neq 0$ and $\gamma_1^L \neq 0$. To ensure the next HWENO reconstruction is stable, we require that the linear weights be positive and their summation equal 1.

Step 3. Compute the smoothness indicators β_l.

The smoothness indicators β_l ($l=0,\dots,3$) measure how smooth the functions $q_l(x)$ in the cell I_i are, and we use the same definition as in the classical WENO scheme [15], i.e.,

$$\beta_l = \sum_{\ell=1}^{r}\int_{I_i}\Delta x^{2\ell-1}\left(\frac{d^\ell q_l(x)}{dx^\ell}\right)^2 dx, \quad l=0,\dots,3,$$

where r is the degree of the polynomials $q_l(x)$. Next, we use a parameter τ_0 to measure the difference between β_0 and β_1 having

$$\tau_0 = (\beta_0-\beta_1)^2,$$

and employ a parameter τ_1 to measure the absolute difference between β_1, β_2 and β_3 as

$$\tau_1 = \left(\frac{|\beta_1-\beta_2|+|\beta_1-\beta_3|}{2}\right)^2.$$

Step 4. Calculate the nonlinear weights.

To combine the polynomials $q_0(x)$ and $q_1(x)$, the nonlinear weights are defined by

$$\omega_l^H = \frac{\bar{\omega}_l^H}{\sum_{\ell=0}^{1}\bar{\omega}_\ell^H}, \quad \text{with } \bar{\omega}_l^H = \gamma_l^H\Big(1+\frac{\tau_0}{\beta_l+\varepsilon}\Big), \quad l=0,1,$$

while for the polynomials $q_1(x)$, $q_2(x)$ and $q_3(x)$, their nonlinear weights are

$$\omega_l^L = \frac{\bar{\omega}_l^L}{\sum_{\ell=1}^{3}\bar{\omega}_\ell^L} \quad \text{with } \bar{\omega}_l^L = \gamma_l^L\Big(1+\frac{\tau_1}{\beta_l+\varepsilon}\Big), \quad l=1,2,3,$$

in which $\varepsilon = 10^{-12}$ is to avoid the zero denominator.

Step 5. Define the final reconstructed polynomial $u_i(x)$ as

$$u_i(x) = \omega_0^H\left(\frac{1}{\gamma_0^H}q_0(x) - \frac{\gamma_1^H}{\gamma_0^H}\tilde{q}_1(x)\right) + \omega_1^H\tilde{q}_1(x),$$

where $\tilde{q}_1(x)$ is defined as

$$\tilde{q}_1(x) = \omega_1^L\left(\frac{1}{\gamma_1^L}q_1(x) - \sum_{l=2}^{3}\frac{\gamma_l^L}{\gamma_1^L}q_l(x)\right) + \sum_{l=2}^{3}\omega_l^L q_l(x).$$

Note that we first replace the linear weights in (2.6) by the nonlinear weights to obtain the HWENO reconstructed polynomial $\tilde{q}_1(x)$, then substitute $q_1(x)$ in (2.5) by $\tilde{q}_1(x)$, and obtain $u_i(x)$ finally using the nonlinear weights ω_0^H and ω_1^H, which makes the HWENO-AO(6,4,2) reconstruction that has the adaptive order resolution when facing discontinuities.

Remark 2.2. The HWENO-AO(6,4,2) reconstruction has the sixth-order accuracy in the smooth regions described in the above steps for that: firstly, we can verify that $\beta_l = O(\Delta x^2)$ and $\beta_1 - \beta_0 = O(\Delta x^3)$ by the Taylor analysis, thus $\tau_0 = O(\Delta x^6)$ and $\omega_l^H = \gamma_l^H + O(\Delta x^4)$, and then

$$\begin{aligned}
u_i(x) - u(x) &= \omega_0^H\left[\frac{1}{\gamma_0^H}q_0(x) - \frac{\gamma_1^H}{\gamma_0^H}\tilde{q}_1(x)\right] + \omega_1^H\tilde{q}_1(x) - u(x)\\
&= (\omega_0^H - \gamma_0^H + \gamma_0^H)\left[\frac{1}{\gamma_0^H}q_0(x) - \frac{\gamma_1^H}{\gamma_0^H}\tilde{q}_1(x)\right] + (\omega_1^H - \gamma_1^H + \gamma_1^H)\tilde{q}_1(x) - u(x)\\
&= (\omega_0^H - \gamma_0^H)\left[\frac{\gamma_0^H + \gamma_1^H}{\gamma_0^H}q_0(x) - \frac{\gamma_1^H}{\gamma_0^H}\tilde{q}_1(x)\right] + (\omega_1^H - \gamma_1^H)\tilde{q}_1(x) + q_0(x) - u(x)\\
&= (\omega_0^H - \gamma_0^H)\left[\frac{\gamma_1^H}{\gamma_0^H}[q_0(x) - \tilde{q}_1(x)] + q_0(x) - u(x)\right] + (\omega_1^H - \gamma_1^H)[\tilde{q}_1(x) - u(x)] + O(\Delta x^6)\\
&= \left[\frac{\gamma_1^H}{\gamma_0^H}[q_0(x) - \tilde{q}_1(x)] + O(\Delta x^6)\right]O(\Delta x^4) + [\tilde{q}_1(x) - u(x)]O(\Delta x^4) + O(\Delta x^6).
\end{aligned}$$

Similarly, we can easily obtain $\tilde{q}_1(x) - u(x) = O(\Delta x^4)$ like the derivation above, then $q_0(x) - \tilde{q}_1(x) = q_0(x) - u(x) + u(x) - \tilde{q}_1(x) = O(\Delta x^4)$, and thus $u_i(x) - u(x) = O(\Delta x^6)$.

(2) The linear approximation for $[\![\partial_x^l u]\!]_{i+1/2}$.

Since we can know the sixth-order linear approximation from the requirement (2.4), $u_{i+1/2}^-$ and $\partial_x u_{i+1/2}^-$ are directly set as $q_0(x_{i+1/2})$ and $q_0'(x_{i+1/2})$, respectively, and then we have

$$[\![\partial_x^l u]\!]_{i+1/2} = q_0^{(l)}(x_{i+1/2})\,|_{I_{i+1}} - q_0^{(l)}(x_{i+1/2})\,|_{I_i}.$$

Note that $q_0(x_{i+1/2})$ has been calculated in the reconstruction of the HWENO scheme, while $[\![\partial_x u]\!]_{i+1/2}$ can be simplified as

$$[\![\partial_x u]\!]_{i+1/2} = \frac{-5\overline{u}_{i-1} + 5\overline{u}_i + 5\overline{u}_{i+1} - 5\overline{u}_{i+2} - 22\overline{v}_{i-1} - 54\overline{v}_i + 54\overline{v}_{i+1} + 22\overline{v}_{i+2}}{36\Delta x}.$$

Hence, this additional procedure only brings a little computation cost compared with the HWENO reconstruction but controls the nonphysical oscillations well, which will be verified in the next numerical tests.

Remark 2.3. The additional damping term in the semi-discrete scheme (2.2) will not destroy the accuracy of the original HWENO scheme for

$$\begin{aligned}
\sigma_i^d &= \omega^d\sum_{l=0}^{1}(2l+1)\Delta x^l([\![\partial_x^l u]\!]_{i-1/2}^2 + [\![\partial_x^l u]\!]_{i+1/2}^2)^{\frac{1}{2}}\\
&= \omega^d[([\![q_0(x)]\!]_{i-1/2}^2 + [\![q_0(x)]\!]_{i+1/2}^2)^{\frac{1}{2}} + 3\Delta x([\![q_0'(x)]\!]_{i-1/2}^2 + [\![q_0'(x)]\!]_{i+1/2}^2)^{\frac{1}{2}}],
\end{aligned}$$

where

$$\llbracket q_0(x)\rrbracket_{i+1/2} = q_0(x_{i+1/2})\,|_{I_{i+1}} - u(x_{i+1/2}) + u(x_{i+1/2}) - q_0(x_{i+1/2})\,|_{I_i} = O(\Delta x^6),$$
$$\llbracket q_0'(x)\rrbracket_{i+1/2} = q_0'(x_{i+1/2})\,|_{I_{i+1}} - u'(x_{i+1/2}) + u'(x_{i+1/2}) - q_0'(x_{i+1/2})\,|_{I_i} = O(\Delta x^5),$$

and thus $\sigma_i^d = \omega^d[[O(\Delta x^{12})+O(\Delta x^{12})]^{\frac{1}{2}} + 3\Delta x[O(\Delta x^{10})+O(\Delta x^{10})]^{\frac{1}{2}}] = O(\Delta x^6)$ in the smooth regions.

(3) Discretization of the semi-discrete scheme (2.2) in time by the third-order TVD Runge-Kutta method [28]:

$$\begin{cases} u^{(1)} = u^n + \Delta t L(u^n), \\ u^{(2)} = \dfrac{3}{4}u^n + \dfrac{1}{4}u^{(1)} + \dfrac{1}{4}\Delta t L(u^{(1)}), \\ u^{n+1} = \dfrac{1}{3}u^n + \dfrac{2}{3}u^{(2)} + \dfrac{2}{3}\Delta t L(u^{(2)}). \end{cases} \tag{2.7}$$

Remark 2.4. For the systems, such as the one-dimensional compressible Euler equations, the HWENO reconstruction at the interface points is performed on the local characteristic directions to avoid the oscillations as the classical WENO scheme [15], while the HWENO reconstruction at the internal points are computed with component by component. In addition, the approximation of $\llbracket \partial_x^l u\rrbracket_{i+1/2}$ is defined in the characteristic field seen in the OFDG scheme [22] for details, which will also add a little computation time as the values in the characteristic field have been calculated in the HWENO reconstruction.

2.2 Two-dimensional case

We first consider two-dimensional scalar hyperbolic conservation laws

$$\begin{cases} u_t + f(u)_x + g(u)_y = 0, \\ u(x,y,0) = u_0(x,y). \end{cases} \tag{2.8}$$

For simplicity, the computing domain is divided by uniform meshes $I_{i,j}=[x_{i-1/2},x_{i+1/2}]\times[y_{j-1/2},y_{j+1/2}]$, in which the mesh sizes $\Delta x = x_{i+1/2} - x_{i-1/2}$ and $\Delta y = y_{j+1/2} - y_{j-1/2}$, and the cell center (x_i, y_j) is $(\frac{x_{i-1/2}+x_{i+1/2}}{2}, \frac{y_{j-1/2}+y_{j+1/2}}{2})$.

To design an OF-HWENO scheme, we first multiply the original governing equation (2.8) by $\frac{1}{\Delta x\Delta y}$, $\frac{x-x_i}{(\Delta x)^2\Delta y}$ and $\frac{y-y_j}{\Delta x(\Delta y)^2}$, respectively, then integrate them over $I_{i,j}$ and employ the numerical fluxes to approximate the fluxes $f(u)$ and $g(u)$ at the interface points. Finally, we add damping terms in the first-order moment equations, respectively, and then obtain the semi-discrete finite volume OF-HWENO scheme as

$$\begin{cases} \dfrac{d\overline{u}_{i,j}(t)}{dt} = -\dfrac{1}{\Delta x\Delta y}\displaystyle\int_{y_{j-1/2}}^{y_{j+1/2}}[\hat{f}(u(x_{i+1/2},y)) - \hat{f}(u(x_{i-1/2},y))]dy \\ \qquad\qquad - \dfrac{1}{\Delta x\Delta y}\displaystyle\int_{x_{i-1/2}}^{x_{i+1/2}}[\hat{g}(u(x,y_{j+1/2})) - \hat{g}(u(x,y_{j-1/2}))]dx, \\ \dfrac{d\overline{v}_{i,j}(t)}{dt} = -\dfrac{1}{\Delta x\Delta y}\displaystyle\int_{x_{i-1/2}}^{x_{i+1/2}}[\hat{g}(u(x,y_{j+1/2})) - \hat{g}(u(x,y_{j-1/2}))]\dfrac{x-x_i}{\Delta x}dx + \dfrac{1}{\Delta x}F_{i,j}(u) \\ \qquad\qquad - \dfrac{1}{2\Delta x\Delta y}\displaystyle\int_{y_{j-1/2}}^{y_{j+1/2}}[\hat{f}(u(x_{i-1/2},y)) + \hat{f}(u(x_{i+1/2},y))]dy - \dfrac{\sigma_{i,j}^{xd}}{\Delta x}\overline{v}_{i,j}(t), \\ \dfrac{d\overline{w}_{i,j}(t)}{dt} = -\dfrac{1}{\Delta x\Delta y}\displaystyle\int_{y_{j-1/2}}^{y_{j+1/2}}[\hat{f}(u(x_{i+1/2},y)) - \hat{f}(u(x_{i-1/2},y))]\dfrac{y-y_j}{\Delta y}dy + \dfrac{1}{\Delta y}G_{i,j}(u) \\ \qquad\qquad - \dfrac{1}{2\Delta x\Delta y}\displaystyle\int_{x_{i-1/2}}^{x_{i+1/2}}[\hat{g}(u(x,y_{j-1/2})) + \hat{g}(u(x,y_{j+1/2}))]dx - \dfrac{\sigma_{i,j}^{yd}}{\Delta y}\overline{w}_{i,j}(t), \end{cases} \tag{2.9}$$

where $\overline{u}_{i,j}(t) = \frac{1}{\Delta x\Delta y}\int_{I_{i,j}} u dxdy$ is the zeroth-order moment, $\overline{v}_{i,j}(t) = \frac{1}{\Delta x\Delta y}\int_{I_{i,j}} u\frac{x-x_i}{\Delta x}dxdy$ and $\overline{w}_{i,j}(t) = \frac{1}{\Delta x\Delta y}\int_{I_{i,j}} u\frac{y-y_j}{\Delta y}dxdy$ are the first-order moments in the x and y directions, respectively,

$\hat{f}(u(x_{i+1/2},y))$ and $\hat{g}(u(x,y_{j+1/2}))$ are the numerical fluxes to approximate the values of $f(u(x_{i+1/2},y))$ and $g(u(x,y_{j+1/2}))$, respectively, $F_{i,j}(u)=\frac{1}{\Delta x\Delta y}\int_{I_{i,j}}f(u)dxdy$ and $G_{i,j}(u)=\frac{1}{\Delta x\Delta y}\int_{I_{i,j}}g(u)dxdy$ are the integral average values for the fluxes $f(u)$ and $g(u)$ over $I_{i,j}$, respectively, and $\sigma_{i,j}^{xd}$ and $\sigma_{i,j}^{yd}$ are the coefficients of the damping terms in the first-order moment equations, respectively.

Here, the integral terms of (2.9) are approximated by the three-point Gaussian quadrature as

$$
\begin{aligned}
&F_{i,j}(u)=\frac{1}{\Delta x\Delta y}\int_{I_{i,j}}f(u)dxdy\approx\sum_{k=1}^{3}\sum_{l=1}^{3}\omega_k\omega_l f(u(x_{G_k},y_{G_l})),\\
&\int_{y_{j-1/2}}^{y_{j+1/2}}\hat{f}(u(x_{i+1/2},y))dy\approx\Delta y\sum_{k=1}^{3}\omega_k\hat{f}(u(x_{i+1/2},y_{G_k})),
\end{aligned}
$$

in which $\omega_1=\frac{5}{18}$, $\omega_2=\frac{4}{9}$ and $\omega_3=\frac{5}{18}$ are the quadrature weights, and the coordinates of the Gaussian points are

$$x_{G_1}=x_{i-\sqrt{15}/10},\quad x_{G_2}=x_i,\quad x_{G_3}=x_{i+\sqrt{15}/10},\quad y_{G_1}=y_{j-\sqrt{15}/10},\quad y_{G_2}=y_j,\quad y_{G_3}=y_{j+\sqrt{15}/10},$$

where x_{i+a} and y_{j+b} denote $x_i+a\Delta x$ and $y_j+b\Delta y$, respectively. The numerical fluxes at the interface points in each direction are taken by the global Lax-Friedrichs numerical fluxes as

$$\hat{f}(u(x,y))=\frac{1}{2}[f(u^-(x,y))+f(u^+(x,y))]-\frac{\alpha}{2}(u^+(x,y)-u^-(x,y))$$

and

$$\hat{g}(u(x,y))=\frac{1}{2}[g(u^-(x,y))+g(u^+(x,y))]-\frac{\beta}{2}(u^+(x,y)-u^-(x,y)),$$

where $\alpha=\max_u|f'(u)|$ and $\beta=\max_u|g'(u)|$. Similarly, $\sigma_{i,j}^{xd}\geqslant 0$ and $\sigma_{i,j}^{yd}\geqslant 0$ satisfying

$$
\begin{aligned}
&\sigma_{i,j}^{xd}=\omega^d\sum_{l=0}^{1}(2l+1)(\Delta x)^l([\![\partial_x^l u]\!]_{i-1/2,j}^2+[\![\partial_x^l u]\!]_{i+1/2,j}^2)^{\frac{1}{2}},\\
&\sigma_{i,j}^{yd}=\omega^d\sum_{l=0}^{1}(2l+1)(\Delta y)^l([\![\partial_y^l u]\!]_{i,j-1/2}^2+[\![\partial_y^l u]\!]_{i,j+1/2}^2)^{\frac{1}{2}},
\end{aligned}
\tag{2.10}
$$

where $[\![\partial_x^l u]\!]_{i+1/2,j}$ and $[\![\partial_y^l u]\!]_{i,j+1/2}$ denote the jumps of $\partial_x^l u(x_{i+1/2},y_j)$ and $\partial_y^l u(x_i,y_{j+1/2})$, respectively. Here, we only consider the zeroth- and first-order partial derivatives of u with respect to x and y variables too, instead of depending on the higher-order partial derivatives of the solution in the OFDG method [23]. ω^d is set as 0.75 for the two-dimensional case, which is not the unique option too, and $\omega^d\in[0.5,1]$ can also be the high resolution with non-oscillatory results for the listed numerical tests. Note that the high-order numerical damping terms are only added in the first-order moment equations, which will not destroy the conservation and accuracy of the scheme and can control spurious oscillations. The explanations are similar to those in the one-dimensional case (see Remarks 2.1 and 2.3 for details).

For the semi-discrete OF-HWENO scheme (2.9), the most important part is the space discretization, including the HWENO reconstruction for the point values of the solutions u at the Gaussian points and the approximation of $[\![\partial_x^l u]\!]_{i\pm1/2,j}$ and $[\![\partial_y^l u]\!]_{i,j\pm1/2}$. Here, the space reconstruction still uses the same polynomials as in the one-dimensional case, and the overall procedures are given as follows.

(1) The HWENO-AO(6,4,2) method for the reconstructed polynomial $u_{i,j}(x,y)$.

Similarly, we add a cubic polynomial as the transition when we construct the HWENO reconstruction method with artificial linear weights, which will automatically have the sixth-, fourth- and second-order resolutions in the different regions, and the associated artificial positive linear weights can be employed with their sum being equal to 1.

Step 1. Reconstruct the approximated polynomials on the different stencils.

We first give the big stencil S_1 in Figure 1. For simplicity, we label the cell $I_{i,j}$ and its neighboring cells as $I_1,\dots,I_9$, and define I_5 as the cell $I_{i,j}$. Then we reconstruct a quintic polynomial $q_0(x,y)$ and a cubic polynomial $q_1(x,y)$ on the big stencil S_1 satisfying

$$\begin{aligned}&\frac{1}{\Delta x\Delta y}\int_{I_k} q_l(x,y)dxdy=\overline{u}_k,\\ &\frac{1}{\Delta x\Delta y}\int_{I_{k_x}} q_l(x,y)\frac{x-x_{k_x}}{\Delta x}dxdy=\overline{v}_{k_x},\quad \frac{1}{\Delta x\Delta y}\int_{I_{k_y}} q_l(x,y)\frac{y-y_{k_y}}{\Delta y}dxdy=\overline{w}_{k_y}\end{aligned}$$

for

$$\begin{aligned}&l=0,\quad k=1,\dots,9,\quad k_x=1,3,4,5,6,7,9,\quad k_y=1,2,3,5,7,8,9;\\ &l=1,\quad k=1,\dots,9,\quad k_x=k_y=5,\end{aligned}$$

where the quintic polynomial $q_0(x,y)$ and the cubic polynomial $q_1(x,y)$ must match the integral average value of u over I_5 to ensure conservation, while match others by a least square methodology as [14]. Later, we give four small stencils $S_2,\dots,S_5$ shown in Figure 2, and then construct four linear polynomials on $S_2,\dots,S_5$, respectively, satisfying

$$\frac{1}{\Delta x\Delta y}\int_{I_k} q_l(x,y)dxdy=\overline{u}_k$$

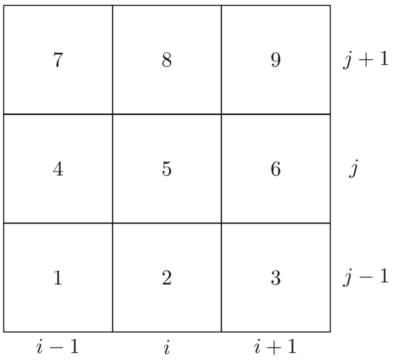

Figure 1 Big stencil S_1

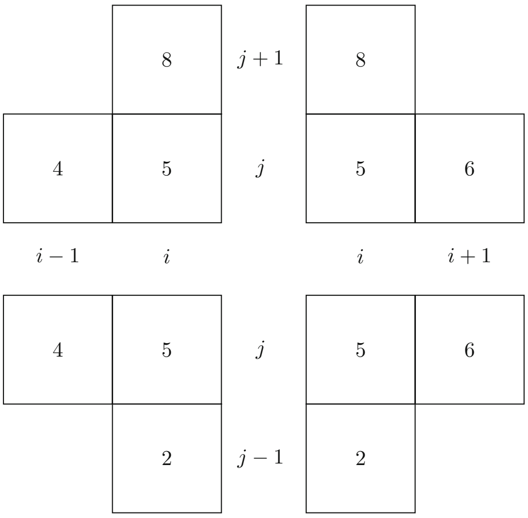

Figure 2 Four small stencils. From left to right and bottom to top: $S_2,\dots,S_5$

for

$$l=2,\quad k=2,4,5;\quad l=3,\quad k=2,5,6,$$
$$l=4,\quad k=4,5,8;\quad l=5,\quad k=5,6,8.$$

Step 2. Obtain equivalent expressions for the above reconstructed polynomials.

We rewrite $q_0(x,y)$ as

$$q_0(x,y)=\gamma_0^H\left(\frac{1}{\gamma_0^H}q_0(x,y)-\frac{\gamma_1^H}{\gamma_0^H}q_1(x,y)\right)+\gamma_1^H q_1(x,y). \tag{2.11}$$

Later, we rewrite $q_1(x,y)$ as

$$q_1(x,y)=\gamma_1^L\left(\frac{1}{\gamma_1^L}q_1(x,y)-\sum_{l=2}^{5}\frac{\gamma_l^L}{\gamma_1^L}q_l(x,y)\right)+\sum_{l=2}^{5}\frac{\gamma_l^L}{\gamma_1^L}q_l(x,y), \tag{2.12}$$

in which the above (2.11) and (2.12) are always satisfied if $\gamma_0^H\neq 0$ and $\gamma_1^L\neq 0$. To ensure the next HWENO procedure is stable, we require that the linear weights be positive with $\sum_{l=0}^{1}\gamma_l^H=1$ and $\sum_{l=1}^{5}\gamma_l^L=1$.

Step 3. Compute the smoothness indicators β_l.

To measure how smooth the functions $q_l(x,y)$ in the target cell $I_{i,j}$ are, we compute the smoothness indicators β_n in the same way as listed by [14], i.e.,

$$\beta_l=\sum_{|\ell|=1}^{r}|I_{i,j}|^{|\ell|-1}\int_{I_{i,j}}\left(\frac{\partial^{|\ell|}}{\partial x^{\ell_1}\partial y^{\ell_2}}q_l(x,y)\right)^2 dxdy,\quad l=0,\dots,5,$$

where $\ell=(\ell_1,\ell_2)$, $|\ell|=\ell_1+\ell_2$ and r is the degree of $q_l(x,y)$. Next, we use a parameter τ_0 to measure the difference between β_0 and β_1 having

$$\tau_0=(\beta_0-\beta_1)^2,$$

and employ a parameter τ_1 to measure the overall difference between β_1 to β_l $(l=2,\dots,5)$ as

$$\tau_1=\left(\frac{\sum_{l=2}^{5}|\beta_1-\beta_l|}{4}\right)^2.$$

Step 4. Calculate the nonlinear weights.

To combine the polynomials $q_0(x,y)$ and $q_1(x,y)$, the nonlinear weights are defined by

$$\omega_l^H=\frac{\bar{\omega}_l^H}{\sum_{\ell=0}^{1}\bar{\omega}_\ell^H}\quad\text{with } \bar{\omega}_l^H=\gamma_l^H\left(1+\frac{\tau_0}{\beta_l+\varepsilon}\right),\quad l=0,1,$$

while for the polynomials $q_1(x),\dots,q_5(x)$, their corresponding nonlinear weights are

$$\omega_l^L=\frac{\bar{\omega}_l^L}{\sum_{\ell=1}^{5}\bar{\omega}_\ell^L}\quad\text{with } \bar{\omega}_l^L=\gamma_l^L\left(1+\frac{\tau_1}{\beta_l+\varepsilon}\right),\quad l=1,\dots,5,$$

in which ε is also taken as 10^{-12} to avoid dividing by zero.

Step 5. Define the final reconstructed polynomial $u_{i,j}(x,y)$ as

$$u_{i,j}(x,y)=\omega_0^H\left(\frac{1}{\gamma_0^H}q_0(x,y)-\frac{\gamma_1^H}{\gamma_0^H}\tilde{q}_1(x,y)\right)+\omega_1^H\tilde{q}_1(x,y),$$

where the $\tilde{q}_1(x,y)$ is defined as

$$\tilde{q}_1(x,y)=\omega_1^L\left(\frac{1}{\gamma_1^L}q_1(x,y)-\sum_{l=2}^{5}\frac{\gamma_l^L}{\gamma_1^L}q_l(x,y)\right)+\sum_{l=2}^{5}\omega_l^L q_l(x,y).$$

Notice that we first replace the linear weights in (2.12) by the nonlinear weights to obtain the HWENO reconstructed polynomial $\tilde{q}_1(x,y)$, then substitute $q_1(x,y)$ in (2.11) by $\tilde{q}_1(x,y)$, and obtain $u_{i,j}(x,y)$ finally by employing the nonlinear weights ω_0^H and ω_1^H, which makes the HWENO-AO(6,4,2) reconstruction that has the adaptive order resolution when facing discontinuities, while also has the sixth-order accuracy in the smooth regions, which are similar to that in the one-dimensional case.

(2) The linear approximation of $[\![\partial_x^l u]\!]_{i+1/2,j}$ and $[\![\partial_y^l u]\!]_{i,j+1/2}$.

As we have known the sixth-order linear approximation for $u_{i,j}(x,y)$ from the above HWENO reconstruction, we directly take $\partial_x^l u_{i+1/2,j}^-$ and $\partial_y^l u_{i,j+1/2}^-$ as $\partial_x^l q_0(x_{i+1/2},y_j)$ and $\partial_y^l q_0(x_i,y_{j+1/2})$, respectively, and then we have

$$[\![\partial_x^l u]\!]_{i+1/2,j} = \partial_x^l q_0(x_{i+1/2},y_j)\,|_{I_{i+1,j}} - \partial_x^l q_0(x_{i+1/2},y_j)\,|_{I_{i,j}}$$

and

$$[\![\partial_y^l u]\!]_{i,j+1/2} = \partial_y^l q_0(x_i,y_{j+1/2})\,|_{I_{i,j+1}} - \partial_y^l q_0(x_i,y_{j+1/2})\,|_{I_{i,j}}.$$

Note that $q_0(x_{i+1/2},y_j)$ and $q_0(x_i,y_{j+1/2})$ have been computed in the reconstruction of the original scheme, while $[\![\partial_x u]\!]_{i+1/2,j}$ and $[\![\partial_y u]\!]_{i,j+1/2}$ can be simplified in advance as the approximation is linear. Similarly, we can also know $\sigma_{i,j}^{xd} = O(\Delta x^6)$ and $\sigma_{i,j}^{yd} = O(\Delta y^6)$ in the smooth regions (see Remark 2.3 for details). Hence, this procedure only adds a bit of computation cost compared with the original scheme, and does not destroy the accuracy of the reconstruction. In addition, it can control spurious oscillations, which will be verified in the next numerical tests.

After we finish the space discretization, the semi-discrete scheme (2.9) is discretized by the third-order TVD Runge-Kutta method (2.7) in time.

Remark 2.5. For the systems, such as the two-dimensional compressible Euler equations, the HWENO reconstruction only at the interface points is performed on the local characteristic directions. In addition, the approximation of $[\![\partial_x^l u]\!]_{i+1/2,j}$ and $[\![\partial_y^l u]\!]_{i,j+1/2}$ is defined in the characteristic field as the OFDG scheme [22], and only adds a little computation cost compared with the original scheme as the values in the characteristic field have been calculated in the HWENO reconstruction. Particularly, we reconstruct the values of the points at $x = x_{i\pm1/2}$ and $y = y_{j\pm1/2}$ in the local characteristic directions provided by $f(u)$ and $g(u)$, respectively.

Remark 2.6. In the damping coefficients (2.3) and (2.10), the weight ω^d is set as 3.5 and 0.75 for one- and two-dimensional cases, respectively. ω^d can also be set as other values, and in the implementation, $\omega^d \in [2,5]$ works well for one dimension, while $\omega^d \in [0.5,1]$ can be the high resolution with non-oscillatory results for two dimensions. If ω^d is in the recommended range, the numerical solution of the OF-HWENO scheme has no obvious difference (see Example 3.8 in Section 3), which means that ω^d is not very sensitive for the resolution and stability. However, we mention that the numerical solution would generate spurious oscillations when ω^d is quite small, and the resolution would be low when ω^d becomes quite large as the high frequency waves are damped out gravely. To some extent, ω^d is still a given parameter artificially, while the resolution depends on the choice of the empirical parameter ω^d, and we think it can be determined by artificial intelligence in the near future.

3 Numerical tests

In this section, we present the numerical results of the OF-HWENO scheme with the artificial linear weights, which is described in Section 2. Meanwhile, we set the linear weights for the lowest degree polynomials as 0.025, while the linear weights for the transition and the highest degree polynomials are the rest. In addition, we also present the numerical results of the modified HWENO (Mo-HWENO) scheme with the artificial linear weights denoted by Zhao and Qiu [36], in which the Mo-HWENO scheme modified the first-order moments in each cell before the space reconstruction, and the linear weights for the lowest degree polynomials are all set as 0.01 as suggested to have a fair comparison. The CFL number is set as 0.45 for all the numerical tests.

Table 1 Total CPU time of St-HWENO and OF-HWENO schemes for Examples 3.1–3.11

Numerical examples	Total CPU time (s)		Increasing
	St-HWENO	OF-HWENO	Rate
Example 3.1 1D Burgers' equation, $t = 0.5/\pi$	2.346E−00	2.532E−00	7.93%
Example 3.2 1D Euler equation, $\rho_0 = 1 + 0.2\sin(\pi x)$	1.286E−01	1.333E−01	3.65%
Example 3.3 2D Burgers' equation, $t = 0.5/\pi$	1.911E−03	2.004E−03	4.87%
Example 3.4 2D Euler equation, $\rho_0 = 1 + 0.2\sin(\pi(x+y))$	2.695E−05	2.717E−05	0.82%
Example 3.5 1D Burgers' equation, $t = 1.5/\pi$	1.539E−03	1.706E−03	10.85%
Example 3.6 1D Lax problem	1.031E−01	1.067E−01	3.49%
Example 3.7 1D Shu-Osher problem	4.704E−01	4.970E−01	5.65%
Example 3.8 1D two blast waves problem	3.586E−00	3.745E−00	4.43%
Example 3.9 2D Burgers' equation, $t = 1.5/\pi$	1.986E−00	2.123E−00	6.90%
Example 3.10 2D double Mach reflection problem	8.403E−04	8.825E−04	5.02%
Example 3.11 2D forward step problem	×	1.944E−05	–

At first, to verify that adding damping terms in the OF-HWENO scheme does bring a little bit of computation time compared with the standard HWENO (the same reconstruction of the OF-HWENO scheme without addition damping terms, St-HWENO) scheme, we list their total CPU time for Examples 3.1–3.11 in Table 1. Overall, the OF-HWENO scheme only adds almost 5% CPU time except in the one-dimensional scalar case, and the OF-HWENO scheme uses less computation time in systems and two-dimensional case than the one-dimensional scalar case compared with the St-HWENO scheme. The reasons are that the reconstruction in the systems is performed on the local characteristic directions, and the reconstruction in the two-dimensional case is also more complicated than that in the one-dimensional case. Note that the total CPU time is also impacted by the time step; therefore, the increasing rate may have a large difference for the smooth tests and non-smooth tests, such as the OF-HWENO scheme adds almost 5% CPU time for 2D double Mach reflection problem, while only adds 0.82% CPU time in the 2D Euler accuracy test, even though they are both modeled by the same governing equations. Certainly, the expense for the calculation of damping terms inevitably has a small increase, but this procedure can maintain the sixth-order accuracy in the smooth regions and control the nonphysical oscillation well near discontinuities simultaneously, which will be both verified in the next numerical tests.

3.1 Accuracy tests

To overcome the oscillations near discontinuities, the OF-HWENO scheme described above brings additional damping terms in the semi-discrete schemes (2.2) and (2.9), which will not destroy the accuracy of the reconstruction. In contrast, the Mo-HWENO scheme modifies the first-order moments before the space reconstruction, which only has the fifth-order accuracy. The detailed results are shown in the accuracy tests below. In addition, we mention that the Mo-HWENO and the OF-HWENO schemes both need a compact three-cell stencil while the classical fifth-order WENO scheme [15] needs a five-cell stencil in the space reconstruction, and in [36], the Mo-HWENO scheme had shown its smaller numerical errors than the classical fifth-order WENO scheme, so we only present the results of the Mo-HWENO scheme here.

Example 3.1. We first solve the following one-dimensional Burgers' equation:

$$u_t + \left(\frac{u^2}{2}\right)_x = 0, \quad 0 < x < 2, \tag{3.1}$$

where $u(x,0) = 0.5 + \sin(\pi x)$ with the periodic boundary conditions, and the final computing time is $t = 0.5/\pi$. At this time, the exact solution is still smooth. In Table 2, we present the numerical errors and orders of the Mo-HWENO and the OF-HWENO schemes. At first, we can know that the Mo-HWENO and the OF-HWENO schemes both achieve the designed fifth- and sixth-order accuracy, respectively, and then we also can find that the OF-HWENO scheme has smaller numerical errors than the Mo-HWENO scheme.

Table 2 1D Burgers' equation: initial data $u(x,0)=0.5+\sin(\pi x)$. Mo-HWENO and OF-HWENO schemes. $t=0.5/\pi$. L^1 and L^∞ errors and orders. N meshes

Meshes	Mo-HWENO scheme				OF-HWENO scheme			
	L^1 error	Order	L^∞ error	Order	L^1 error	Order	L^∞ error	Order
30	7.73E−05		6.88E−04		6.34E−06		7.05E−05	
60	1.35E−06	5.84	2.11E−05	5.03	8.61E−08	6.20	1.41E−06	5.64
90	1.64E−07	5.19	2.73E−06	5.04	7.19E−09	6.12	1.44E−07	5.64
120	3.82E−08	5.07	6.05E−07	5.24	1.20E−09	6.22	2.57E−08	5.98
150	1.23E−08	5.09	1.98E−07	5.01	3.02E−10	6.19	6.39E−09	6.24
180	4.89E−09	5.06	7.71E−08	5.17	1.02E−10	5.97	2.00E−09	6.37

Example 3.2. We have the following one-dimensional Euler equations:

$$\frac{\partial}{\partial t}\begin{pmatrix}\rho\\ \rho\mu\\ E\end{pmatrix}+\frac{\partial}{\partial x}\begin{pmatrix}\rho\mu\\ \rho\mu^2+p\\ \mu(E+p)\end{pmatrix}=0, \tag{3.2}$$

where ρ is the density, μ is the velocity, E is the total energy and p is the pressure. Initial conditions: $\rho(x,0)=1+0.2\sin(\pi x)$, $\mu(x,0)=1$, $p(x,0)=1$ and $\gamma=1.4$. Boundary conditions: period. Computing domain: $[0,2]$. Final computing time: $t=2$. The exact solution is $\rho(x,t)=1+0.2\sin(\pi(x-t))$, $\mu(x,0)=1$ and $p(x,0)=1$. We present the numerical errors and orders of the density for the Mo-HWENO and the OF-HWENO schemes in Table 3, and then we can see that the OF-HWENO scheme has the sixth-order accuracy with smaller numerical errors, while the Mo-HWENO scheme only has the fifth-order accuracy.

Example 3.3. We now solve the following two-dimensional Burgers' equation:

$$u_t+\left(\frac{u^2}{2}\right)_x+\left(\frac{u^2}{2}\right)_y=0,\quad 0<x<4,\quad 0<y<4, \tag{3.3}$$

where $u(x,y,0)=0.5+\sin(\pi(x+y)/2)$ with periodic boundary conditions in each direction. The final computing time is $t=0.5/\pi$, in which the solution is still smooth. In Table 4, we present the numerical errors and orders of the Mo-HWENO and the OF-HWENO schemes, which illustrates that the OF-HWENO scheme has higher-order accuracy and smaller numerical errors than the Mo-HWENO scheme.

Example 3.4. We have the following two-dimensional Euler equations:

$$\frac{\partial}{\partial t}\begin{pmatrix}\rho\\ \rho\mu\\ \rho\nu\\ E\end{pmatrix}+\frac{\partial}{\partial x}\begin{pmatrix}\rho\mu\\ \rho\mu^2+p\\ \rho\mu\nu\\ \mu(E+p)\end{pmatrix}+\frac{\partial}{\partial y}\begin{pmatrix}\rho\nu\\ \rho\mu\nu\\ \rho\nu^2+p\\ \nu(E+p)\end{pmatrix}=0, \tag{3.4}$$

Table 3 1D Euler equations: initial data $\rho(x,0)=1+0.2\sin(\pi x)$, $\mu(x,0)=1$ and $p(x,0)=1$. Mo-HWENO and OF-HWENO schemes. $t=2$. L^1 and L^∞ errors and orders. N meshes

Meshes	Mo-HWENO scheme				OF-HWENO scheme			
	L^1 error	Order	L^∞ error	Order	L^1 error	Order	L^∞ error	Order
30	1.06E−06		3.04E−06		3.86E−09		7.19E−09	
40	2.52E−07	4.99	5.27E−07	6.09	5.41E−10	6.83	9.69E−10	6.97
50	8.25E−08	5.01	1.59E−07	5.36	1.16E−10	6.88	2.06E−10	6.95
60	3.31E−08	5.00	5.87E−08	5.47	3.30E−11	6.92	5.76E−11	6.98
70	1.53E−08	5.00	2.63E−08	5.20	1.13E−11	6.93	1.97E−11	6.96
80	7.85E−09	5.00	1.31E−08	5.23	4.49E−12	6.93	7.77E−12	6.97

Table 4 2D Burgers' equation: initial data $u(x,y,0)=0.5+\sin(\pi(x+y)/2)$. Mo-HWENO and OF-HWENO schemes. $t=0.5/\pi$. L^1 and L^∞ errors and orders. $N_x\times N_y$ meshes

Meshes	Mo-HWENO scheme				OF-HWENO scheme			
	L^1 error	Order	L^∞ error	Order	L^1 error	Order	L^∞ error	Order
30×30	3.47E−05		1.59E−04		1.86E−05		2.30E−04	
60×60	7.68E−07	5.50	8.88E−06	4.17	4.43E−07	5.39	5.89E−06	5.29
90×90	9.98E−08	5.03	1.33E−06	4.68	3.57E−08	6.21	5.48E−07	5.86
120×120	2.35E−08	5.03	3.15E−07	5.02	5.46E−09	6.52	8.45E−08	6.50
150×150	7.78E−09	4.95	1.05E−07	4.93	1.24E−09	6.66	1.90E−08	6.70
180×180	3.13E−09	4.99	4.20E−08	5.00	3.67E−10	6.67	5.83E−09	6.47

Table 5 2D Euler equations: initial data $\rho(x,y,0)=1+0.2\sin(\pi(x+y))$, $\mu(x,y,0)=1$, $\nu(x,y,0)=1$ and $p(x,y,0)=1$. Mo-HWENO and OF-HWENO schemes. $t=2$. L^1 and L^∞ errors and orders. $N_x\times N_y$ meshes

Meshes	Mo-HWENO scheme				OF-HWENO scheme			
	L^1 error	Order	L^∞ error	Order	L^1 error	Order	L^∞ error	Order
20×20	1.59E−05		4.20E−05		2.37E−06		4.64E−06	
40×40	5.00E−07	4.99	8.83E−07	5.57	1.87E−08	6.99	3.85E−08	6.92
60×60	6.58E−08	5.00	1.08E−07	5.17	1.13E−09	6.92	2.28E−09	6.97
80×80	1.56E−08	5.00	2.51E−08	5.08	1.53E−10	6.95	3.06E−10	6.98
100×100	5.12E−09	5.00	8.13E−09	5.05	3.24E−11	6.97	6.70E−11	6.81
120×120	2.06E−09	5.00	3.25E−09	5.03	9.64E−12	6.64	2.05E−11	6.50

where ρ is the density, (μ,ν) is the velocity, E is the total energy, and p is the pressure. Initial conditions: $\rho(x,y,0)=1+0.2\sin(\pi(x+y))$, $\mu(x,y,0)=1$, $\nu(x,y,0)=1$, $p(x,y,0)=1$ and $\gamma=1.4$. Computing domain: $[0,2]\times[0,2]$. The boundary conditions are periodic in each direction, and the computing time is $t=2$. The exact solution of ρ is $\rho(x,y,t)=1+0.2\sin(\pi(x+y-2t))$. We give the numerical errors and orders of the density for the Mo-HWENO and the OF-HWENO schemes in Table 5, and then we can find that the OF-HWENO scheme not only has higher-order accuracy but also has smaller numerical errors.

3.2 Non-smooth tests

To verify whether the damping terms for the first-order moment equations in the OF-HWENO scheme are necessary or not, we will partly present the numerical results of the St-HWENO scheme, and the results illustrate that the damping terms in the OF-HWENO scheme can improve the stability and enhance the resolution simultaneously.

Example 3.5. We now solve the one-dimensional Burgers' equation (3.1) given in Example 3.1 with the same initial and boundary conditions, but the computing time is $t=1.5/\pi$, where the solution is discontinuous. We present the numerical solution of the Mo-HWENO and the OF-HWENO schemes against the exact solution in Figure 3, and the performances are similar with high resolutions for the two HWENO schemes.

Example 3.6. We solve the Lax problem with the following Riemann initial condition:

$$(\rho,\mu,p,\gamma)^{\mathrm{T}}=\begin{cases}(0.445,0.698,3.528,1.4)^{\mathrm{T}}, & x\in[-0.5,0),\\(0.5,0,0.571,1.4)^{\mathrm{T}}, & x\in[0,0.5],\end{cases}$$

which is modeled by the one-dimensional Euler equation (3.2), and the final computing time is 0.16. In Figure 4, we plot the exact solution against the computed density ρ and its partially enlarged view obtained by the HWENO schemes, which shows that the St-HWENO scheme has slight oscillations. In contrast, the Mo-HWENO and the OF-HWENO schemes both keep good resolutions with non-oscillations, which illustrates that the damping term in the first-order moment equation for the

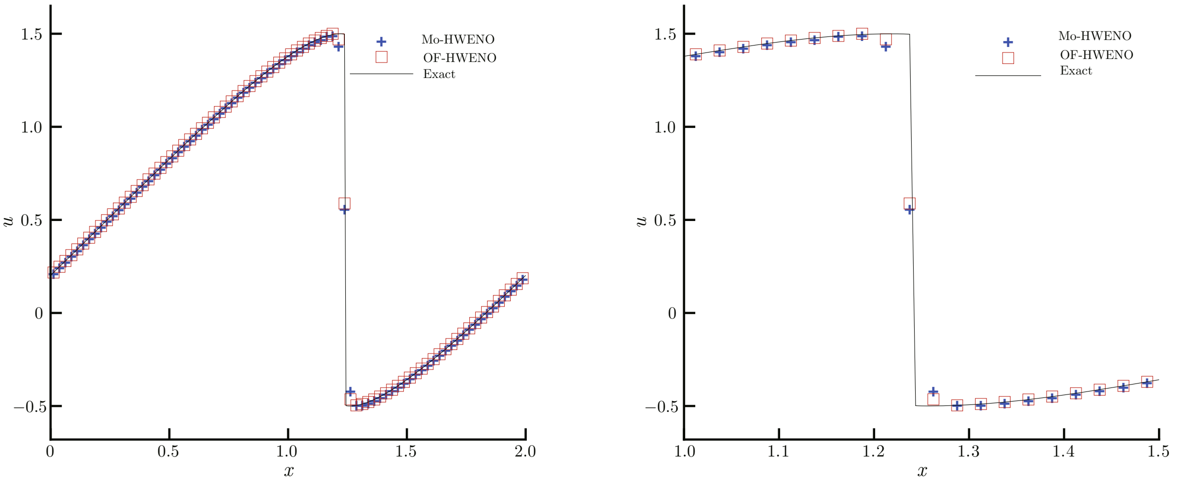

(a) Numerical results (b) Partially enlarged view of (a)

Figure 3 (Color online) 1D Burgers' equation: initial data $u(x,0)=0.5+\sin(\pi x)$. $t=1.5/\pi$. Black solid line: the exact solution; blue plus signs: the results of the Mo-HWENO scheme; red squares: the results of the OF-HWENO scheme. 80 meshes

OF-HWENO scheme has similar effect with the modification for the first-order moment in the Mo-HWENO scheme. In addition, if we do not modify the first-order moment in the Mo-HWENO scheme, the results have obvious oscillations, which illustrates that the adaptive order HWENO reconstruction in the OF-HWENO scheme has better performance than that in the Mo-HWENO scheme.

Example 3.7. We solve the Shu-Osher problem [26], and the initial condition is

$$(\rho,\mu,p,\gamma)^{\mathrm{T}}=\begin{cases}(3.857143, 2.629369, 10.333333, 1.4)^{\mathrm{T}}, & x\in[-5,-4),\\ (1+0.2\sin(5x), 0, 1, 1.4)^{\mathrm{T}}, & x\in[-4,5],\end{cases}$$

which is also modeled by the one-dimensional Euler equation (3.2). This problem has a moving Mach equal to 3 shock interaction with sine waves in the density, which is a typical example containing shocks and complex smooth region structures simultaneously. The final computing time is 1.8, and we show the numerical results of the computed density ρ and the partially enlarged view in Figure 5, where the referenced "exact" solution is obtained by the fifth-order finite difference WENO scheme [15] with 2,000 grid points. We can see that the OF-HWENO scheme has higher resolutions than the St-HWENO and the Mo-HWENO schemes. Since the damping term can reduce the singularities of the first-order moment equation, the OF-HWENO scheme would use more information provided by the highest degree polynomial in the reconstruction near the extreme points. In other words, the damping term can enhance the resolution and perform better than the modification of the first-order moments in the Mo-HWENO scheme. In addition, if we do not modify the first-order moment in the Mo-HWENO scheme, it fails for the simulation even using a smaller CFL number, which shows that the adaptive order HWENO reconstruction in the OF-HWENO scheme is more robust than that in the Mo-HWENO scheme.

Example 3.8. We solve the interaction of the two blast waves problem, and the initial condition is

$$(\rho,\mu,p,\gamma)^{\mathrm{T}}=\begin{cases}(1,0,10^3,1.4)^{\mathrm{T}}, & 0<x<0.1,\\ (1,0,10^{-2},1.4)^{\mathrm{T}}, & 0.1<x<0.9,\\ (1,0,10^2,1.4)^{\mathrm{T}}, & 0.9<x<1,\end{cases}$$

where the reflective boundary condition is applied here, and the final computing time is 0.038. In Figure 6, we plot the computed density against the reference "exact" solution and the zoomed one, in which the "exact" solution is also computed by the fifth-order finite difference WENO scheme [15] with 2,000 grid points. The OF-HWENO scheme also has better performance than the other two HWENO schemes, and the St-HWENO scheme has obvious oscillations, which illustrates that the damping term can enhance the resolution and overcome the oscillations in the OF-HWENO scheme simultaneously. In addition, we mention that the Mo-HWENO scheme has lower resolutions, which may be that the HWENO modification for the first-order moments uses more information provided by the two linear polynomials (see [36]), while the OF-HWENO scheme does not rely on the test cases since its damping term is approximated by a linear method. Similarly, when we do not modify the first-order moment in the Mo-HWENO scheme, it fails in simulating the test even by employing a smaller CFL number, which illustrates that the adaptive order HWENO reconstruction in the OF-HWENO scheme has better performance than that in the Mo-HWENO scheme.

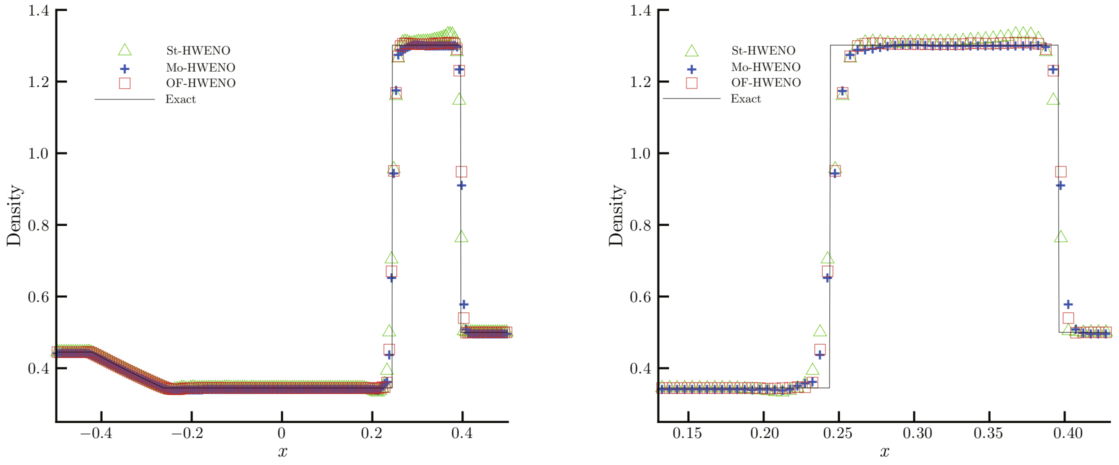

(a) Numerical results of the computed density

(b) Partially enlarged view of (a)

Figure 4 (Color online) Lax problem. $t = 0.16$. Black solid line: the exact solution; green triangles: the results of the St-HWENO scheme; blue plus signs: the results of the Mo-HWENO scheme; red squares: the results of the OF-HWENO scheme. 200 meshes

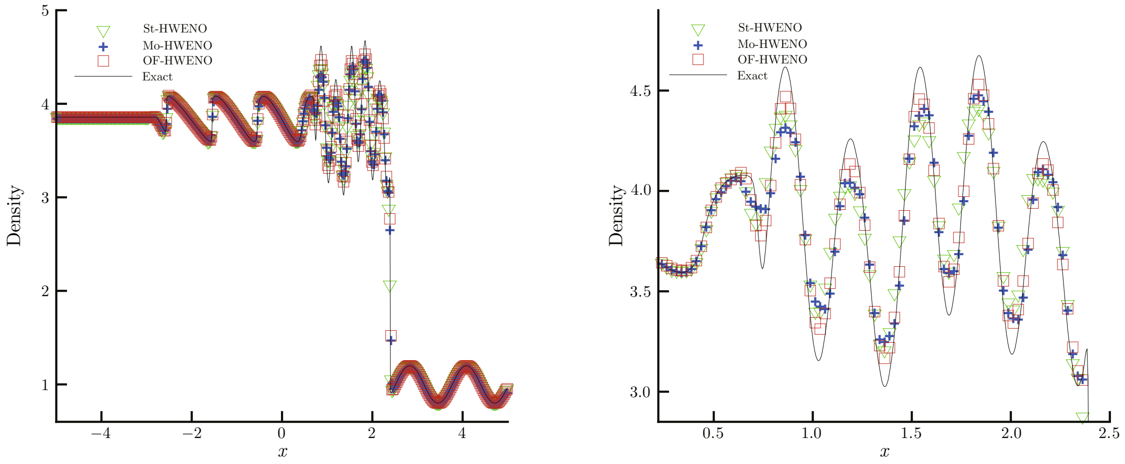

(a) Numerical results of the computed density

(b) Partially enlarged view of (a)

Figure 5 (Color online) Shu-Osher problem. $t = 1.8$. Black solid line: the exact solution; green triangles: the results of the St-HWENO scheme; blue plus signs: the results of the Mo-HWENO scheme; red squares: the results of the OF-HWENO scheme. 400 meshes

Moreover, to investigate the sensitivity of the weight ω^d in (2.3) for the resolution and stability of the OF-HWENO scheme, we present the density computed by the OF-HWENO scheme with a different coefficient on the range of $[2, 5]$ in Figure 7, and we can see that the results are quite similar with the high resolution. Particularly, the symbol "3" represents the results of the OF-HWENO scheme in the case of $\omega^d = 3.5$, and $\omega^d = 3.5$ is also the recommended weight for one-dimensional problems. Hence, we can know that when ω^d is in the recommended range, the OF-HWENO scheme is not very sensitive to the resolution of the numerical solution. But we still want to mention that quite small ω^d would make the OF-HWENO scheme have spurious oscillations, while quite large ω^d would obtain a low resolution.

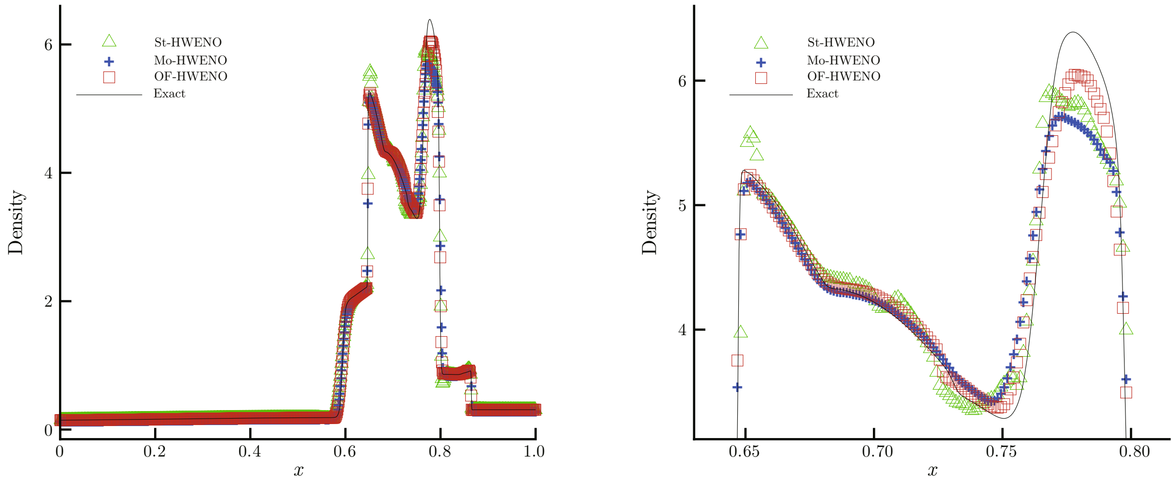

(a) Numerical results of the computed density (b) Partially enlarged view of (a)

Figure 6 (Color online) Two blast waves problem. $t = 0.038$. Black solid line: the exact solution; green triangles: the results of the St-HWENO scheme; blue plus signs: the results of the Mo-HWENO scheme; red squares: the results of the OF-HWENO scheme. 800 meshes.

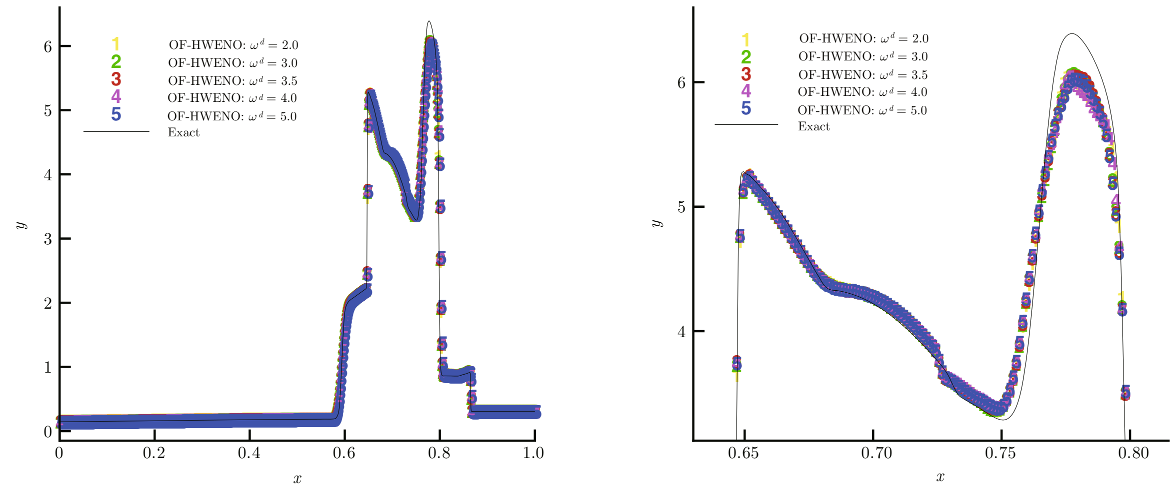

(a) Numerical results of the computed density (b) Partially enlarged view of (a)

Figure 7 (Color online) Two blast waves problem. $t = 0.038$. Different weights ω^d in the damping coefficient for the OF-HWENO scheme. Black solid line: the exact solution; yellow "1": $\omega^d = 2.0$; green "2": $\omega^d = 3.0$; red "3": $\omega^d = 3.5$; purple "4": $\omega^d = 4.0$; blue "5": $\omega^d = 5.0$. 800 meshes

Example 3.9. We then solve the two-dimensional Burgers' equation (3.3) given in Example 3.3 with the same initial and boundary conditions, while the final computing time is $1.5/\pi$, in which the solution has discontinuities. In Figure 8, we give the numerical results computed by the Mo-HWENO and the OF-HWENO schemes, their partially enlarged view, and the surface of the numerical solution by the OF-HWENO scheme, and then we can see that the two HWENO schemes have similar results with high resolutions.

Example 3.10. We next solve the double Mach reflection problem [30], which is modeled by the two-dimensional Euler equation (3.4), and the computation domain is $[0,4]\times[0,1]$. This problem contains a reflection wall, which lies at the bottom from $x=\frac{1}{6}$ and $y=0$, but has a 60° angle in terms of the x-axis. Hence, the reflection boundary condition is applied for the bottom boundary except in the part from $x=0$ to $x=\frac{1}{6}$, which imposes the exact post-shock condition, and it also has an exact moving Mach 10 shock in the top boundary. The final computing time is 0.2. In Figure 9, we plot the pictures of the region $[0,3]\times[0,1]$ and the blow-up region around the double Mach stems, then we can see that the Mo-HWENO and the OF-HWENO schemes have high resolutions around the double Mach stems, and the OF-HWENO scheme can capture more fine structure seemingly.

Example 3.11. Later, we solve the problem of an initial right-going Mach 3 wind tunnel with a step [30], which is also modeled by the two-dimensional Euler equation (3.4). The wind tunnel has a width of 1 unit and a length of 3 units, while the step has a height of 0.2 units located at 0.6 length units from the left of the tunnel. Reflective boundary conditions are applied along the wall of the tunnel, while the in-flow and the out-flow boundary conditions are applied on the left and right boundaries, respectively. The final computing time is $t=4$. In Figure 10, we present the density computed by the Mo-HWENO and the OF-HWENO schemes showing that the OF-HWENO scheme has higher resolutions. In addition, the St-HWENO scheme cannot work in this test even if we adjust the linear weights, which illustrates that the damping terms in the OF-HWENO scheme have significant effects to control spurious oscillations and thus make the scheme robust.

Example 3.12. We now solve the 80 Mach number astrophysical jet problem, where the Mach number of the jet in-flow is Mach 25 with respect to the sound speed in the light ambient gas and Mach 80 with respect to the sound speed in the heavy jet gas is initialized without the radiative cooling. It is a challenging problem for simulating the gas and shocks discovered by the Hubble space telescope, which had been simulated using the positivity-preserving technique [33]. In this test, we use the positivity-preserving technique [10, 33] and use the exponential Runge-Kutta method in the first-order moment equations as was done in the OFDG method [22] to overcome the quite large jump of the damping term. The computational domain is $[0,2]\times[-0.5,0.5]$, and the entire domain is full of the ambient gas with

$$(\rho,\mu,\nu,p,\gamma)^{\mathrm{T}}=(0.5,0,0,0.4127,5/3)^{\mathrm{T}}$$

initially. In the left boundary, $(\rho,\mu,\nu,p,\gamma)^{\mathrm{T}}$ are set as $(5,30,0,0.4127,5/3)^{\mathrm{T}}$ for $y\in[-0.05,0.05]$ and taken as $(0.5,0,0,0.4127,5/3)^{\mathrm{T}}$ otherwise. The out-flow conditions are applied for the right, the top, and the bottom boundaries. The final computing time is $t=0.07$. In Figure 11, we show the density and pressure computed by the OF-HWENO scheme, and we obtain similar results comparing [22,33]. Here, we mention that the damping term in the first-order moment equations for the proposed OF-HWENO scheme can make the numerical solution essential non-oscillations, but it cannot make the solution positivity-preserving. The reason is that the damping term is mainly used to reduce the singularities from the first-order moment equations near discontinuities, but this technique has no restrictions for the high-degree polynomials in the reconstruction. Hence, for this extremal problem with quite strong shocks, the positivity-preserving technique [33] is a necessary procedure for the proposed OF-HWENO scheme, and it was also used in the positivity-preserving HWENO scheme [10] for compressible Navier-Stokes equations.

Example 3.13. We next solve the Sedov point blast problem [33]. The initial conditions are: $\rho=1$, $\mu=0$, $\nu=0$, $E=10^{-12}$, $\gamma=1.4$ everywhere, but the energy is set as $\frac{0.244816}{\Delta x\Delta y}$ only in the cell at the left bottom corner. The computing time is $t=1$. In this test, we also use the positivity-preserving technique [10,33] and the exponential Runge-Kutta method as that in the OFDG method [22] to avoid the negative pressure or density, which are two necessary procedures to make the OF-HWENO scheme stable when facing quite strong shocks. In Figure 12, we present the density computed by the OF-HWENO scheme, and we obtain similar results comparing [22, 33].

Example 3.14. We finally solve the shock refection problem, which is a steady state problem, and had been solved directly using unsteady Euler equations in [40]. The computational domain is $[0,4]\times[0,1]$. The reflection and supersonic out-flow boundary conditions are applied in the bottom and right, respectively. For others, Dirichlet boundary conditions are set as

$$(\rho,\mu,\nu,p,\gamma)^{\mathrm{T}}=\begin{cases}(1.0,2.9,0.0,1.0/1.4,1.4)^{\mathrm{T}}\,|_{(0,y,t)^{\mathrm{T}}},\\(1.69997,2.6193,-0.50632,1.52819,1.4)^{\mathrm{T}}\,|_{(x,1,t)^{\mathrm{T}}}.\end{cases}$$

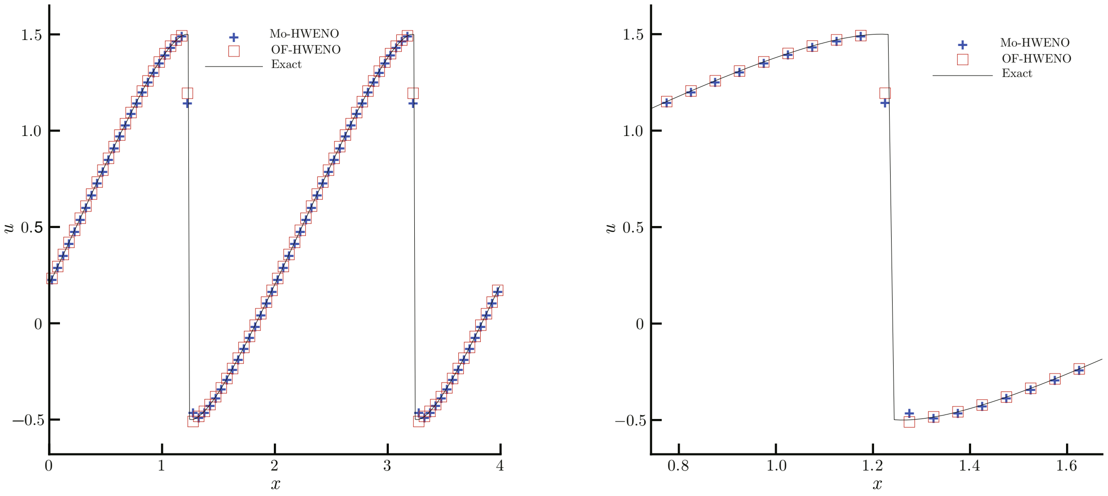

(a) Numerical solution at $x=y$

(b) Partially enlarged view of (a)

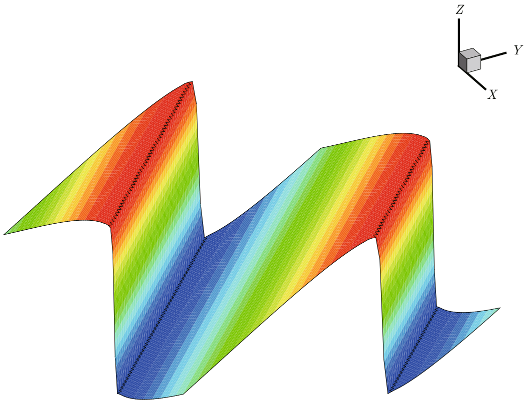

(c) Surface of u for OF-HWENO

Figure 8 (Color online) 2D Burgers' equation: initial data $u(x,y,0)=0.5+\sin(\pi(x+y)/2)$. $t=1.5/\pi$. Black solid line: the exact solution; blue plus signs: the results of the Mo-HWENO scheme; red squares: the results of the OF-HWENO scheme. 80×80 meshes

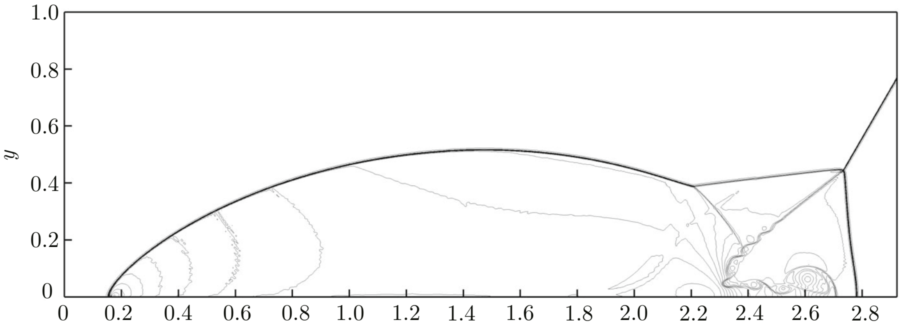

(a) Density contours computed by Mo-HWENO

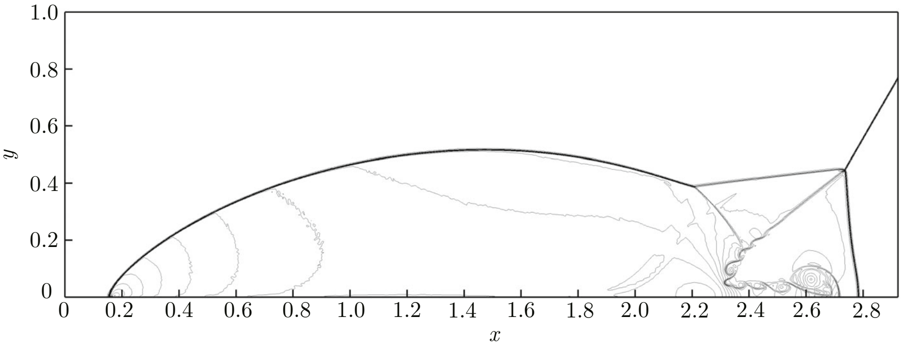

(b) Density contours computed by OF-HWENO

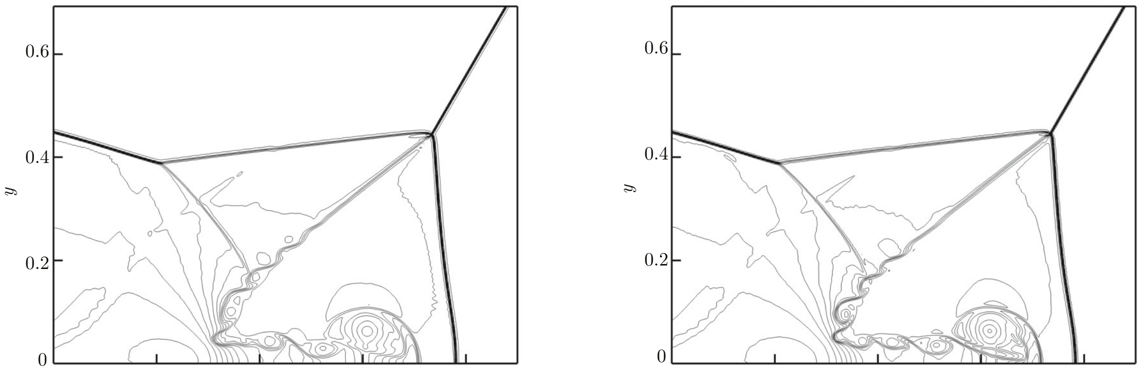

(c) Zoom-in picture for (a) (d) Zoom-in picture for (b)

Figure 9 (Color online) Double Mach reflection problem. $t = 0.2$. 30 equally spaced density contours from 1.5 to 22.7. 1,600 × 400 meshes

The left boundary conditions are applied as the initial conditions in the entire domain. In Figure 13, we present the density and the average residue computed by the OF-HWENO scheme and the St-HWENO scheme (the proposed HWENO scheme without the damping term). We can first see that the OF-HWENO scheme has a smaller average residue than the St-HWENO scheme, but their average residue cannot be close to the machine zero. Meanwhile, the numerical solution of the St-HWENO scheme generates obvious oscillation, while the only difference between the two HWENO schemes is the usage of the damping term. It means that the damping term in the OF-HWENO scheme plays an important role in controlling spurious oscillations, and makes the solutions have better convergence.

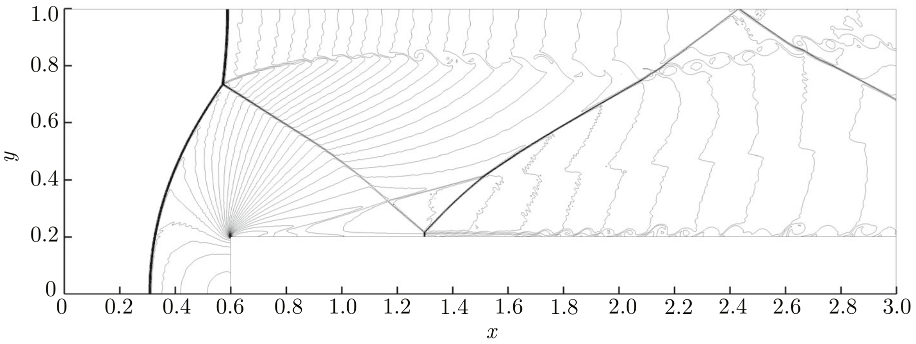

(a) Density contours computed by Mo-HWENO

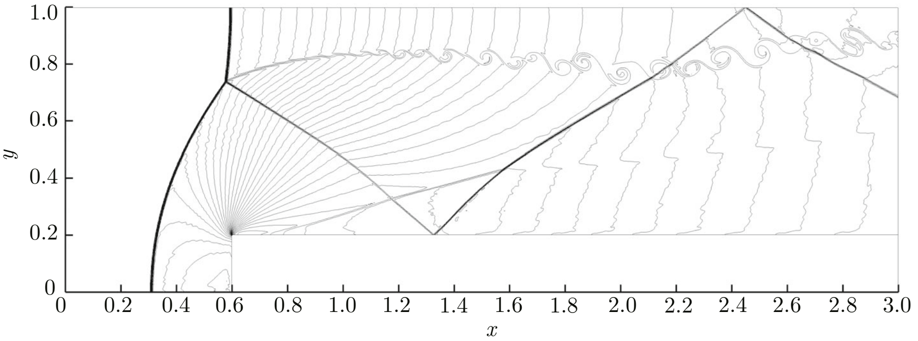

(b) Density contours computed by OF-HWENO

Figure 10 (Color online) Forward step problem. $t = 4$. From left to right: 30 equally spaced density contours from 0.32 to 6.15. 960×320 meshes

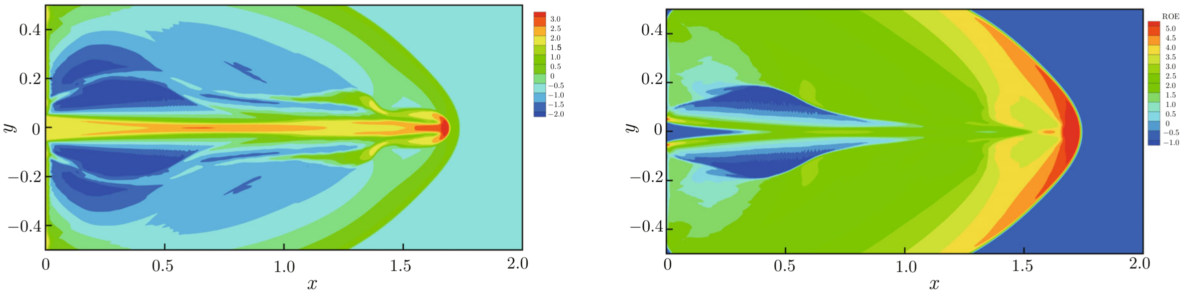

(a) Logarithmic density contours (b) Logarithmic pressure contours

Figure 11 (Color online) 80 Mach number astrophysical jet problem. $t = 0.07$. Numerical results of the OF-HWENO scheme. 448×224 meshes

4 Concluding remarks

In this paper, a sixth-order finite volume moment-based oscillation-free Hermite weighted essentially non-oscillatory (OF-HWENO) scheme with artificial linear weights is designed for hyperbolic conservation laws. Compared with other moment-based HWENO schemes [19,35,36], the OF-HWENO scheme achieves the highest theoretical order accuracy, which yields smaller numerical errors and higher-order accuracy. In order to have the adaptive order resolution near discontinuities, we add a transition polynomial in the HWENO reconstruction, which is more robust than that in [36], where the associated linear weights can also be any positive numbers (their sum is one). The main difference of the OF-HWENO scheme from other HWENO schemes is that the scheme modifies the first-order moment equations by adding damping terms, which does not destroy the conservation and accuracy firstly and can control spurious

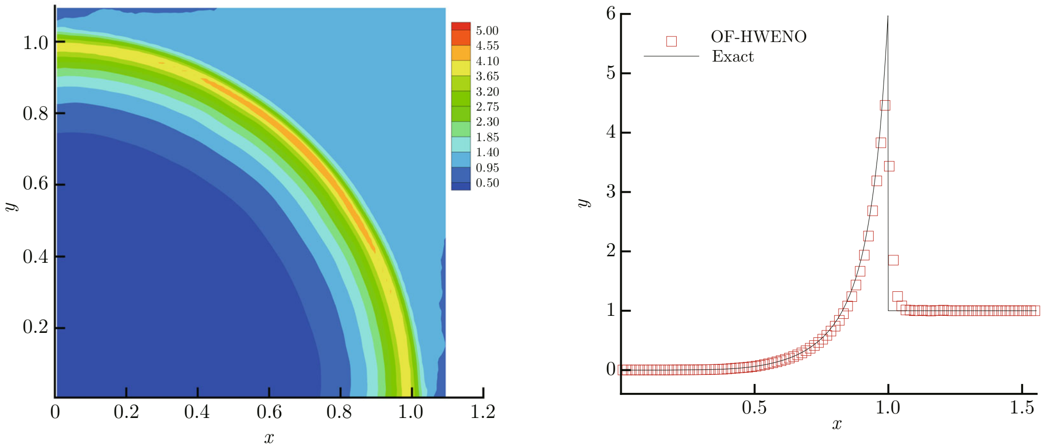

(a) Density contours (b) Density projected to the radical coordinates

Figure 12 (Color online) Sedov point blast problem. $t = 1$. Numerical results of the OF-HWENO scheme. 100×100 meshes

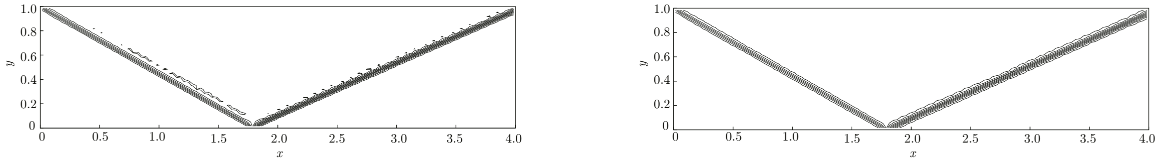

(a) Density contours computed by St-HWENO (b) Density contours computed by OF-HWENO

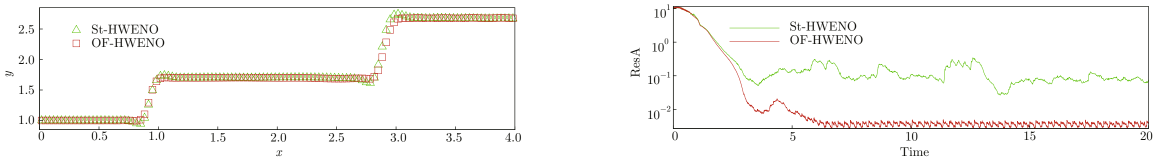

(c) Density distribution along line $y = 0.5$ (d) evolution of the average residue

Figure 13 (Color online) Shock refection problem. $t = 20$. 15 equally spaced density contours from 1.10 to 2.58. 120×30 meshes

oscillations and enhance resolutions while only adding a little computation cost as the approximation for the damping terms is linear. Meanwhile, the OF-HWENO scheme is easy to implement using the same reconstructed polynomials directly in the space discretization. In addition, the OF-HWENO scheme uses more compact stencils and achieves higher-order accuracy than the classical fifth-order WENO scheme [15]. In general, the OF-HWENO scheme has a compact stencil, high-order accuracy, high resolution, and non-physical oscillations simultaneously, which are all shown in the numerical results above. The extension of the method to unstructured meshes is going on.

For more challenging problems, such as the 80 Mach number astrophysical jet problem and the Sedov point blast problem, the proposed OF-HWENO scheme cannot simulate it directly unless adding the positivity-preserving technique [10, 33]. Meanwhile, for the problems with strong shocks, there is a quite large jump in the damping term, which would make the time step quite small. To relax the time restriction from the damping term, we also apply the exponential Runge-Kutta method in the first-order moment equations as was done in the OFDG method [22]. For the steady state problems, if we directly use the OF-HWENO scheme by solving unsteady Euler equations, the average residue of the scheme still cannot be close to the machine zero. There are no published HWENO schemes to solve unsteady Euler equations and obtain steady state solutions, and we will consider it by modifying the nonlinear weights in the near future.

Acknowledgements Jianxian Qiu was supported by National Key R&D Program of China (Grant No. 2022YFA1004501). Zhuang Zhao was supported by the Postdoctoral Science Foundation of China (Grant No. 2021M702145). The authors thank Chair Professor Shi Jin at Shanghai Jiao Tong University for his helpful comments on the paper, and the first author Zhuang Zhao also thanks PhD Candidates Jiayin Li and Chuan Fan at Xiamen University for helpful discussions in the numerical implementation.

References

1 Balsara D S, Garain S, Florinski V, et al. An efficient class of WENO schemes with adaptive order for unstructured meshes. J Comput Phys, 2020, 404: 109062

2 Balsara D S, Garain S, Shu C-W. An efficient class of WENO schemes with adaptive order. J Comput Phys, 2016, 326: 780–804

3 Becker R, Braack M. A two-level stabilization scheme for the Navier-Stokes equations. In: Numerical Mathematics and Advanced Applications. Berlin-Heidelberg: Springer, 2004, 123–130

4 Braack M, Burman E. Local projection stabilization for the Oseen problem and its interpretation as a variational multiscale method. SIAM J Numer Anal, 2006, 43: 2544–2566

5 Cai X F, Zhang X X, Qiu J X. Positivity-preserving high order finite volume HWENO schemes for compressible Euler equations. J Sci Comput, 2016, 68: 464–483

6 Castro M, Costa B, Don W S. High order weighted essentially non-oscillatory WENO-Z schemes for hyperbolic conservation laws. J Comput Phys, 2011, 230: 1766–1792

7 Cockburn B, Shu C-W. TVB Runge-Kutta local projection discontinuous Galerkin finite element method for conservation laws II: General framework. Math Comp, 1989, 52: 411–435

8 Costa B, Don W S. Multi-domain hybrid spectral-WENO methods for hyperbolic conservation laws. J Comput Phys, 2007, 224: 970–991

9 Dumbser M, Balsara D S, Toro E F, et al. A unified framework for the construction of one-step finite volume and discontinuous Galerkin schemes on unstructured meshes. J Comput Phys, 2008, 227: 8209–8253

10 Fan C, Zhang X X, Qiu J X. Positivity-preserving high order finite volume hybrid Hermite WENO schemes for compressible Navier-Stokes equations. J Comput Phys, 2021, 445: 110596

11 Harten A. Preliminary results on the extension of ENO schemes to two-dimensional problems. In: Proceedings of International Conference on Nonlinear Hyperbolic Problems. Lecture Notes in Mathematics, vol. 1270. Berlin: Springer-Verlag, 1987, 23–40

12 Harten A, Engquist B, Osher S, et al. Uniformly high order accurate essentially non-oscillatory schemes, III. J Comput Phys, 1987, 71: 231–323

13 Harten A, Osher S. Uniformly high-order accurate nonoscillatory schemes. SIAM J Numer Anal, 1987, 24: 279–309

14 Hu C Q, Shu C-W. Weighted essentially non-oscillatory schemes on triangular meshes. J Comput Phys, 1999, 150: 97–127

15 Jiang G-S, Shu C-W. Efficient implementation of weighted ENO schemes. J Comput Phys, 1996, 126: 202–228

16 Levy D, Puppo G, Russo G. Central WENO schemes for hyperbolic systems of conservation laws. ESAIM Math Model Numer Anal, 1999, 33: 547–571

17 Levy D, Puppo G, Russo G. Compact central WENO schemes for multidimensional conservation laws. SIAM J Sci Comput, 2000, 22: 656–672

18 Li J Y, Shu C-W, Qiu J X. Multi-resolution HWENO schemes for hyperbolic conservation laws. J Comput Phys, 2021, 446: 110653

19 Li J Y, Shu C-W, Qiu J X. Moment-based multi-resolution HWENO scheme for hyperbolic conservation laws. Commun Comput Phys, 2022, 32: 364–400

20 Liu H X, Qiu J X. Finite difference Hermite WENO schemes for hyperbolic conservation laws. J Sci Comput, 2015, 63: 548–572

21 Liu X D, Osher S, Chan T. Weighted essentially non-oscillatory schemes. J Comput Phys, 1994, 115: 200–212

22 Liu Y, Lu J F, Shu C-W. An essentially oscillation-free discontinuous Galerkin method for hyperbolic systems. SIAM J Sci Comput, 2022, 44: A230–A259

23 Lu J F, Liu Y, Shu C-W. An oscillation-free discontinuous Galerkin method for scalar hyperbolic conservation laws. SIAM J Numer Anal, 2021, 59: 1299–1324

24 Qiu J X, Shu C-W. Hermite WENO schemes and their application as limiters for Runge-Kutta discontinuous Galerkin method: One-dimensional case. J Comput Phys, 2004, 193: 115–135

25 Qiu J X, Shu C-W. Hermite WENO schemes and their application as limiters for Runge-Kutta discontinuous Galerkin method II: Two dimensional case. Comput & Fluid, 2005, 34: 642–663

26 Shu C-W. Essentially non-oscillatory and weighted essentially non-oscillatory schemes for hyperbolic conservation laws. In: Advanced Numerical Approximation of Nonlinear Hyperbolic Equations. Lecture Notes in Mathematics, vol. 1697. Berlin-Heidelberg: Springer, 1998, 325–432

27 Shu C-W. Essentially non-oscillatory and weighted essentially non-oscillatory schemes. Acta Numer, 2020, 29: 701–762

28 Shu C-W, Osher S. Efficient implementation of essentially non-oscillatory shock capturing schemes. J Comput Phys, 1988, 77: 439–471

29 Tao Z J, Li F F, Qiu J X. High-order central Hermite WENO schemes: Dimension-by-dimension moment-based reconstructions. J Comput Phys, 2016, 318: 222–251

30 Woodward P, Colella P. The numerical simulation of two-dimensional fluid flow with strong shocks. J Comput Phys, 1984, 54: 115–173

31 Yanuar I W, Kosasih E A. Fifth-order Hermite targeted essentially non-oscillatory schemes for hyperbolic conservation laws. J Sci Comput, 2021, 87: 69

32 Zahran Y H, Abdalla A H. Seventh order Hermite WENO scheme for hyperbolic conservation laws. Comput & Fluid, 2016, 131: 66–80

33 Zhang X X, Shu C-W. On positivity-preserving high order discontinuous Galerkin schemes for compressible Euler equations on rectangular meshes. J Comput Phys, 2010, 229: 8918–8934

34 Zhang Y T, Shu C-W. Third order WENO scheme on three dimensional tetrahedral meshes. Commun Comput Phys, 2009, 5: 836–848

35 Zhao Z, Chen Y B, Qiu J X. A hybrid Hermite WENO scheme for hyperbolic conservation laws. J Comput Phys, 2020, 405: 109175

36 Zhao Z, Qiu J X. A Hermite WENO scheme with artificial linear weights for hyperbolic conservation laws. J Comput Phys, 2020, 417: 109583

37 Zheng N Y, Cai X F, Qiu J-M, et al. A conservative semi-Lagrangian hybrid Hermite WENO scheme for linear transport equations and the nonlinear Vlasov-Poisson system. SIAM J Sci Comput, 2021, 43: A3580–A3606

38 Zhu J, Qiu J X. A class of the fourth order finite volume Hermite weighted essentially non-oscillatory schemes. Sci China Ser A, 2008, 51: 1549–1560

39 Zhu J, Qiu J X. A new fifth order finite difference WENO scheme for solving hyperbolic conservation laws. J Comput Phys, 2016, 318: 110–121

40 Zhu J, Shu C-W. Numerical study on the convergence to steady state solutions of a new class of high order WENO schemes. J Comput Phys, 2017, 349: 80–96

41 Zhu J, Shu C-W. A new type of multi-resolution WENO schemes with increasingly higher order of accuracy. J Comput Phys, 2018, 375: 659–683